広島市立大学審査博士学位論文

Theory of nonlinearities in cochlear mechanics

計算モデルに基づく蝸牛非線形現象の解明

2015年9月

広島市立大学大学院
情報科学研究科　博士後期課程
情報科学専攻

村上 泰樹

Abstract

This research investigates how active and nonlinear mechanisms generate nonlinear phenomena in the cochlea using a computational model.

The cochlea acts as a frequency analyzer in the human auditory system. This process is realized by active and nonlinear cochlear mechanics. Improving our understanding of the cochlear mechanics requires us to investigate our hearing system. Experimental research can directly explain mechanics; however, cochlear mechanics cannot currently be accurately measured because the cochlear structure is fine and elaborate. Instead of an experimental approach, modeling studies have the potential to uncover cochlear mechanics, especially if they can be described by basic physical principles. Moreover, active and nonlinear systems like these have been previously analyzed in many science and engineering fields.

Typical cochlear nonlinearities include compression, two-tone suppression (2TS) and distortion product. The first nonlinearity involves nonlinear growth in a cochlear IO function, the second nonlinearity is the reduction in cochlear response for a tone when another tone is presented, and the third nonlinearity is the generation of a cochlear response for absent tones where multiple tones are presented. This thesis focuses on the above three cochlear nonlinearities.

To investigate the mechanisms of these cochlear nonlinearities, a transmission line model including an active and nonlinear element was developed. The transmission line model is described by basic physical principles. The active and nonlinear element is inspired from isolated outer hair cell (OHC) findings.

The nonlinear responses obtained from the transmission line model can account for the experimental measurements, and is generated by the active and nonlinear OHC model, which is the only active and nonlinear element in the cochlear model. Consequently, the analysis of the OHC model is key to understanding the cochlear nonlinearities. The results of the analysis of the OHC model also show similar properties to those of the cochlear model. Therefore, it is suggested that the active and nonlinear OHC mechanisms generate these nonlinearities in the cochlear mechanics.

Acknowledgments

This thesis would not have been possible without the help from many individuals. I would like to acknowledge all of the people who in their won way helped and supported me with the present work.

I would like to acknowledge my thesis advisor, Professor Shunsuke Ishimitsu, for his outstanding guidance, encouragement, and support, throughout the course of this work.

I would like to acknowledge Professor Yasuhide Kobayashi, Professor Satoshi Iwaki, as two members of my thesis committee, for their invaluable suggestions and comments in my study.

I would like to acknowledge Professor Masato Akagi at Japan Advance Institute of Science and Technology, as a member of my thesis committee, for their invaluable suggestions and discussion in my study at early stages. I also would like to thank for his invaluable comments to improve the quality of this thesis.

I would like to acknowledge Professor Hatsuo Hayashi at Kyushu Institute of Technology and Professor Masashi Unoki at Japan Advance Institute of Science and Technology for their invaluable suggestions and discussion in my study at early stages.

I would like to acknowledge Professor Stephen Elliott at Institute of Sound and Vibration Research, University of Southampton, United Kingdom for his fruitful discussions and constructive suggestions in my study.

I would like to thank Dr. Yuzo Takahashi and Dr. Masashi Nakayama at for their help and discussions in my study.

I would like to thank all members of the Sound Design Laboratory at Hiroshima City University.

I would like to thank my parents for their support during my pursuit of a doctoral degree.

Contents

List of Figures

List of Tables

Chapter 1

Introduction

In recent years, with an increase in computer processing capacity, computers have rapidly become ubiquitous in many areas of human endeavor. In humans, our perception of hearing is instant and easy; however, the tasks that we take for granted are difficult for a computer. For optimal computer performance, an approach based on a combination of psychoacoustics and speech perception creates a high quality speech synthesis system, and a statistical approach to speech data produces an excellent automatic speech recognition system. However, these systems focus on speech sounds, and processing these sounds is complicated.

We hear many kinds of sounds, not only speech sounds, in the natural environment. Moreover, our hearing is part of human activity. For that reason, this thesis considers that our hearing system understands sound using a few underlying rules. Given this, what are the key elements of these underlying rules?

This thesis focuses on a bottom-up approach to understanding our hearing. Hearing processing consists of hearing organs and the brain. Sound waves pass the hearing organs with mechanical vibrations, and the brain processes sound information using neural codes. The cochlea performs the role of converting sound waves into neural firing. Hence, one function of the cochlea in hearing is time–frequency analysis. Hydro and mechanical dynamics realize the decomposition of incoming sound waves to frequency information, and electrophysiological dynamics convert mechanical information into neural information in the cochlea. The cochlea's mechanical dynamics in particular are well known to be nonlinear. Furthermore, the results of cochlear processing cannot be predicted easily. Direct measurement of mechanical dynamics in the cochlea is the most effective way to understand cochlear function, but it is difficult to measure the total mechanical response from a structure that is both complicated and sensitive to surgical injuries.

The mechanisms of the cochlea are still wrapped in mystery. From the point of view of computer science, the cochlea can be considered to be an active and nonlinear system. Thus, computational modeling studies, rather than direct measurements, have the potential to unveil the underlying active and nonlinear cochlear mechanisms.

1.1 Cochlear mechanics

The fundamental parameters of sound are amplitude, frequency and phase, which vary across time. This information is processed during hearing for the perception and recognition of sound. Our hearing can perceive an amplitude range of 120 dB, from 20 μPa to 20 Pa of sound pressure level, and a frequency range of 20 Hz to 20 kHz. These ranges for sound pressure level and frequency indicate great abilities. The cochlea plays the important role of frequency analysis in this process. Also, Fourier transform is well known as a frequency analysis method and is commonly used in many scenes. However, before the proposal of Fourier transform, our hearing had realized the frequency analysis by the cochlea.

The cochlea's structure takes the form of a coiled tube filled with fluid. The basilar membrane (BM) divides the cochlear tube into two rooms, and is lined with sensor cells. The incoming sound wave vibrates the BM mechanically; the patterns of this BM vibration depend on the sound frequency. For lower frequency sounds, the BM vibration occurs at the entrance of the cochlea. In contrast, the BM vibration is generated at the apex of the cochlea for higher frequency sounds. This idea was proposed by Helmholtz in the late 19th century [1], and half a century later, von Békésy observed the frequency dependence of the BM's mechanical vibration in cadavers, and discovered the cochlea's frequency analysis mechanism [2]. In addition, his observation pointed out a unique vibration that is well known as the traveling wave. The pattern of the traveling wave in the BM moves from the entrance to the apex, and its amplitude is at a maximum at the resonance point. However, the tuning of the BM resonance is lower than that of the auditory nerve (AN) firing that results from the sensor cells' processing on the BM (*e.g.,* Ref. [3]). In the 1980s, BM vibrations were observed in living animals and showed similarly shaped tuning properties of AN firing and higher amplitudes of BM vibration than those in the dead cochlea [4]. More recently, BM and AN in the same cochlea were found to have equivalent frequency tuning properties [5].

Consequently, the question arises as to how the living cochlea produces the sharp frequency tuning and the high amplitude of the BM response.

Many investigators have commonly believed that active mechanisms underlie the cochlear mechanics to produce the sharp frequency tuning and the high amplitude of the BM response. This active mechanisms idea is supported by isolated cell experiments *in vivo*. In these experiments, the outer hair cell (OHC) sensor cell showed active motion toggled by stimuli to the cell. The shape of the OHC consists of a cell body and sensory hairs called the hair bundle. The intracellular potential of the cell body is 70 mV in a resting state, and varies with the hair bundle displacement. This variation depends on whether mechanical channels regulating the ionic flow at the apex of the hair bundle are open or closed by the hair bundle displacement, and the variation of ionic flow causes the variation of the intracellular potential of the cell body. This phenomenon indicates that the OHC transforms mechanical BM motion into electronic motion. Furthermore, the length of the OHC's cell body is changed by intracellular potential [6, 7], a phenomenon that is called somatic motility. After the discovery of somatic motility, it was thought to boost the BM motion in a cycle-by-cycle action (*e.g.,* Ref. [8]). When the 21th century came over, the somatic motility disappeared mice was proposed, and showed the sharp frequency tuning and the higher amplitude of BM motion [9]. Further, another active OHC motion called the hair bundle motility has also been observed *in vivo* [10]. This motility consists of the force generation of the hair bundle mechanisms toggled by its displacement; it is possible that the force generated by the hair bundle mechanisms produces the sharp frequency tuning and the higher amplitude of BM motion [11]. Both of the somatic and hair bundle mechanisms have advantages and disadvantages; however, recent work shows that both are necessary for the cochlear mechanism [12]. As a direct consequence of these experimental results, the cochlear mechanics in living hearing are thought to be active.

The function of the active mechanisms is not only the generation of the sharp frequency tuning and the higher amplitude of BM motion. It is commonly believed that the active process is a source of nonlinearities in the cochlear mechanics. Understanding these nonlinearities is useful to clarify our understanding of the cochlea, because nonlinearity causes difficulties in detection systems. Three typical cochlear nonlinearities are observed in BM motion, AN firing, cochlear monophonic, oto-acoustic emission (OAE), and psychological measurements.

- **Compression**

  The cochlear input–output (IO) function shows a nonlinear curve. At lower and higher input levels, the IO curve grows linearly. At a moderate input level, the slope of the IO curve is less than 1 dB/dB. This nonlinear growth is called compression. In BM motion, the degree of compression is lower than 0.2 dB/dB at a characteristic frequency (CF) that is the most sensitive frequency at a longitudinal location of the cochlea and becomes linear when the sound frequency is well above the CF [13, 14]. Psychological measurements show similar IO curves; however, they have a lower degree of compression over 0.4 dB/dB [15].

- **Two-tone suppression**

  BM motion for a tone is reduced when a stronger tone is inputted. This reduction is called two-tone suppression (2TS). The dominant and suppressed tones are called the suppressor and probe, respectively. This 2TS phenomenon, first observed in the AN half a century ago [16], has also been detected in the BM [17] and the inner hair cells (IHCs) [18] within the past two decades. Ref. [17] concluded that 2TS originates from mechanical phenomena at the BM and is generated by active processes.

- **Distortion product**

  Distortion products (DPs) are a response to an absent tone after a two-tone pair is transmitted to the hearing apparatus. This phenomenon was observed 50 years ago in the AN [19], in OAEs [20], and on the BM [21, 22].

The somatic motility disappeared mice did not show the cochlear nonlinearities [9, 23, 24, 25]. The reason for this is that the active processes of the OHCs, alongside the hair bundle mechanisms, are related to the cochlear nonlinearities. However, it is still unclear how the active processes generate the cochlear nonlinearities. This result has led to the obstruction of understanding in hearing studies.

1.2 Cochlear modeling

An alternative method to experimental studies is the use of modeling studies, as experiments can run into technical difficulties; however, this is not the only reason to use them. Modeling studies have the potential to clarify common mechanisms in some phenomena and to explain mechanisms without noise.

Current cochlear models can be categorized as either transmission line models or phenomenological models. The former describe the mechanical dynamics in the cochlea, while the latter focus on the cochlear IO properties. Cochlear modelers choose either a transmission line model or a phenomenological model, depending on their study.

Transmission line model

After Békésy's discovery, hydrodynamics in the theoretical treatment of cochlear sound propagation became an important way to explain the BM vibration pattern known as the traveling wave. In the transmission line model, the cochlea is considered to be an uncoiled duct structure with two fluid-filled compartments whose walls, separated by the BM, are rigid [26, 27]. By applying fundamental physical principles, the basic equations for the transmission line model are obtained and can be illustrated by an equivalent electrical circuit. This passive model can well reproduce the BM traveling wave obtained from the dead cochlea.

To produce the sharp frequency tuning and higher amplitude of BM motion in the living cochlea, the simplest way is to increase the Q factor at each BM location. This higher Q factor can reproduce the amplitude of BM motion. However, the frequency tuning property generated by this higher Q factor is sharper than the results obtained from the experimental measurements. To solve this problem, active models were proposed [28, 29, 30]. In those models, active elements at base of the peak of the BM traveling wave boost BM vibration, and produce sharper frequency tuning and higher amplitude of BM motion.

These active elements are necessary for explaining living cochlear mechanics. Also, the cochlear nonlinearities could be accounted for by nonlinear transmission line models [31, 32, 33, 34, 35, 36, 37]. These models incorporate a nonlinear element that is also active. The basic idea behind the nonlinear mechanisms in the models is that the active and nonlinear element boosts BM motion at a lower sound pressure level, and this amplification is saturated over a moderate sound pressure level.

Phenomenological model

Békésy's discovery inspired the phenomenological modeling of the cochlea. The most successive phenomenological concept is a bandpass filter bank that represents cochlear processing [38]. This filter bank concept is based on the fact that the

resonance of the BM depends on the CF. The width of the bandpass filter is decided by the frequency tuning properties of the BM, and is calculated from psychological measurements.

Active and nonlinear phenomenological models of the cochlea have been proposed to account for the cochlear nonlinearities [39, 40]. These models are designed using digital signal processing. The basic idea of the nonlinear filter bank model is to vary the shape of the bandpass filter with sound pressure level. At lower sound pressure levels, the width of the bandpass filter is the shaper. Over a moderate sound pressure level, the width of the bandpass filter becomes broader depending on the sound pressure level. Moreover, the value of the gain factor in the model is reduced by increasing the sound pressure level.

1.3 Research objectives

The aim of this thesis is to improve our understanding of the nonlinearities in the cochlear mechanics using a modeling study.

As already mentioned, the cochlea analyzes the frequency of the sound before the human brain perceives it. This analysis can process various sounds, from soft to loud and from low-pitched to high-pitched. Furthermore, the active and nonlinear processes in the cochlea produce this analysis in an elaborate way. Isolated cell experiments have shown active and nonlinear processes in the OHC; however, a gap exists between the isolated OHC findings and the actual cochlear mechanics.

This thesis concentrates on using a model to investigate how the active and nonlinear processes generate the cochlear nonlinearities. To do this, we propose a one-dimensional transmission line model of the cochlea, including an active and nonlinear element inspired from the isolated OHC findings. This work is motivated by the fact that the transmission line model should be derived from fundamental physical principles. Consequently, results obtained from the transmission line model can account for the cochlear mechanics. In this thesis, we focus on three typical cochlear nonlinearities: compression, two-tone suppression (2TS) and DP.

1.4 Organization of the thesis

This thesis consists of seven chapters. A schematic overview of this thesis is presented in Fig. 1.1.

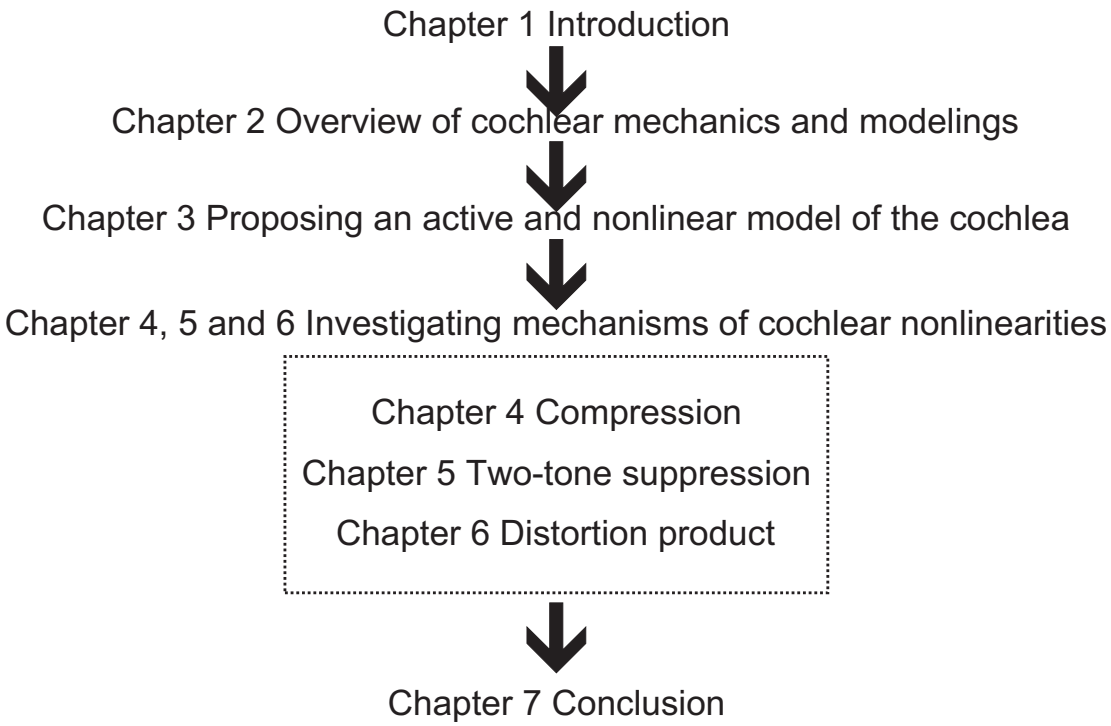

Figure 1.1: Thesis construction

- **Chapter 2** starts with the description of the peripheral auditory system consisting of the outer ear, the middle ear and the cochlea. The description is divided into two parts: structures and responses.
- **Chapter 3** proposes a transmission line model of the cochlea, including an active and nonlinear element.
- **Chapter 4, 5, and 6** investigate the mechanisms of compression, two-tone suppression and DP, respectively, within the active and nonlinear transmission line model of the cochlea.
- **Chapter 7** summarizes this thesis and suggests further studies.

Chapter 2

Overview of cochlear mechanics

The human hearing system consists of the outer, middle and inner ear. The cochlea is included in the inner ear. First, sound waves propagating in the external field are collected by the outer ear. Then, the collected sound is carried into the cochlea by the middle ear, which matches the impedance between the air and the cochlear fluid. If the impedance is not matched, then the cochlea reflects sound waves back to the outer ear. Finally, the inputted sound wave is transformed into neural firing by the cochlea. Auditory perception and cognition are based on this neural information in our brain.

This chapter provides an overview of the cochlear mechanics. As the path through which sound travels, the outer and middle ear have important roles. In Section 2.1, some anatomical and physiological features are introduced. To understand the basics of cochlear mechanics, Section 2.2 introduces anatomical features of the cochlea. In Section 2.3, mechanical and neural features of the cochlea are introduced. Furthermore, some psychological experimental results that might describe these features are outlined. Section 2.4 introduces psychological findings related to cochlear function.

2.1 Anatomy and function of outer and middle ear

Figure 2.1 shows the periphery of the human ear. The auditory periphery consists of the outer, middle and inner ear. The incoming sound travels through the pinna, concha, ear canal and eardrum, and the resonance of the concha and ear canal produce the sound pressure at the eardrum. The complex structure of the pinna provides directionality cues to aid in sound localization.

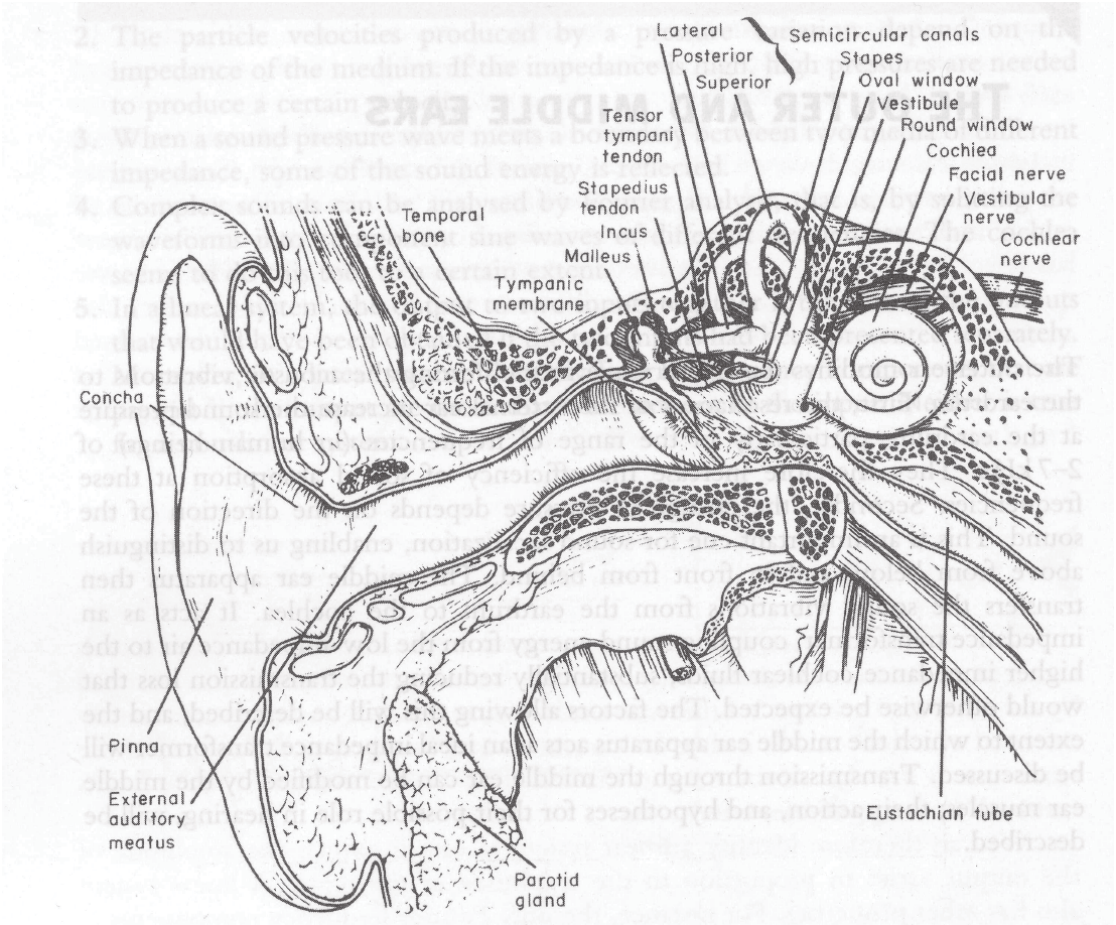

Figure 2.1: The external, middle and inner ears in humans. From Pickles [41], Fig. 2.1.

The middle ear couples sound energy from the ear canal to the cochlea, and by its transformer action helps to match the impedance of the ear canal to the much higher impedance of the cochlear fluids. In the absence of a transformer mechanisms, much of the sound would be reflected. The middle ear consists of a chain of three small bones: the malleus, the incus and the stapes, shown in Fig. 2.1. The first two bones are joined comparatively rigidly so that when the tip of the malleus is pushed by the tympanic membrane, the bones rotate together and transfer the force to the stapes. The stapes is attached to a flexible window in the wall of the cochlea, known as the oval window.

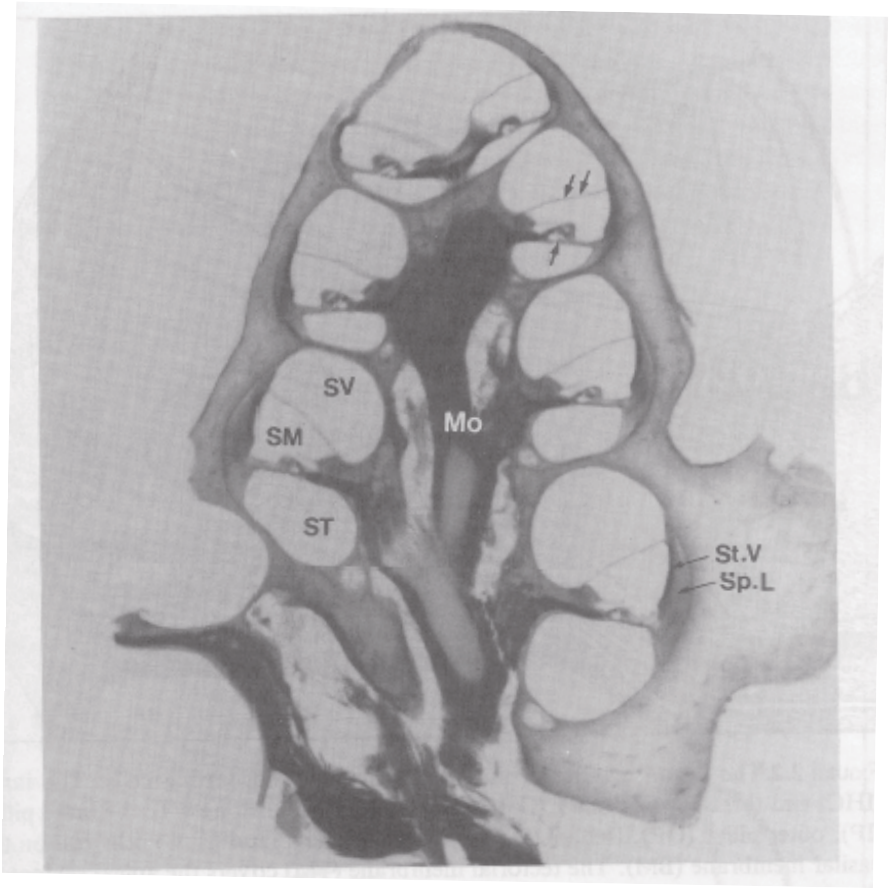

Figure 2.2: Cross section of the cochlea. From Slepecky [42], Fig. 2.1. SV: Scala vestibuli, SM: Scala media, ST: Scala tympani and Mo: MODIOLUS

2.2 Structure of cochlea

The structure of the cochlea is a coiled tube. The width of the human cochlea is about 10 mm, and its height is about 5 mm. Figure 2.2 displays a cross section of the coiled cochlea to show detail of the cochlea's turns and the three cochlear rooms: the upper, middle and lower rooms are called the scala vestibuli, the scala media, and the scala tympani, respectively. The scala vestibuli and the scala media are divided by Reissner's membrane, and the scala media and the scala tympani are divided by the BM, which is 35 mm in length. The scala vestibuli and the scala tympani are connected at the apex of the cochlea.

The sound transmitted via the middle ear vibrates the oval window connecting to the scala vestibuli at the entrance of the cochlea and generates a pressure difference between the scala vestibuli and the scala tympani. The width of the BM varies with longitudinal direction: it is narrower at the cochlear base and

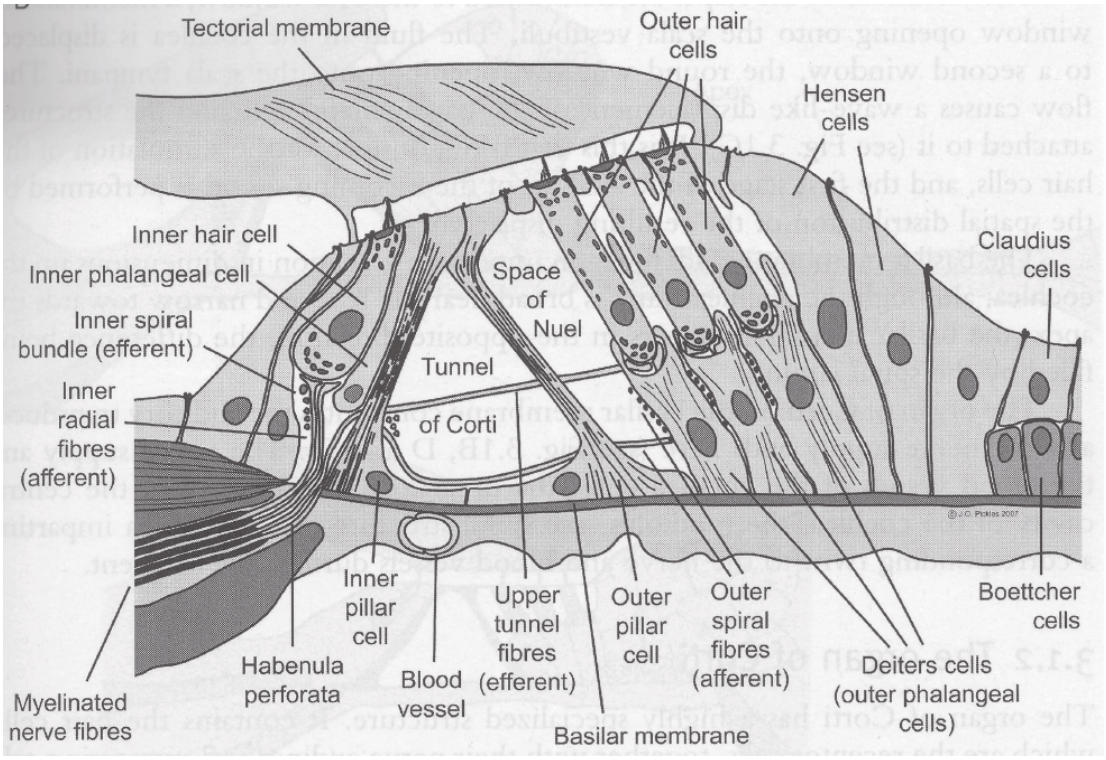

Figure 2.3: Cross section of the organ of Corti. From Pickles [41], Fig. 3.1(D).

broader at the cochlear apex. This variation is caused by the gradual distribution of the BM natural frequency.

The organ of Corti consists of sensor cells (called hair cells), ANs, and supporting cells, as shown in Fig. 2.3. The hair cells are divided into the IHCs and the OHCs, which are located on one and three rows, respectively. The organ of Corti is covered by the tectorial membrane (TM). The apices of the OHCs are attached to the TM; however, the apices of the IHCs are not attached to the TM. Shared motion of the TM directly affects the OHCs. It is considered that IHCs are affected by fluid injection when shared motion of the TM is generated.

2.3 Response of cochlea

The sound transmitted via the middle ear strikes the oval window at the entrance of the cochlea, as shown in Fig. 2.4 (top). This vibration causes the vibration of cochlear fluid and the BM. As a result, a vibration called the BM traveling wave propagates from the base to the apex of the cochlea. The peak of the BM traveling wave depends on the sound frequency, as shown in Fig. 2.4 (middle).

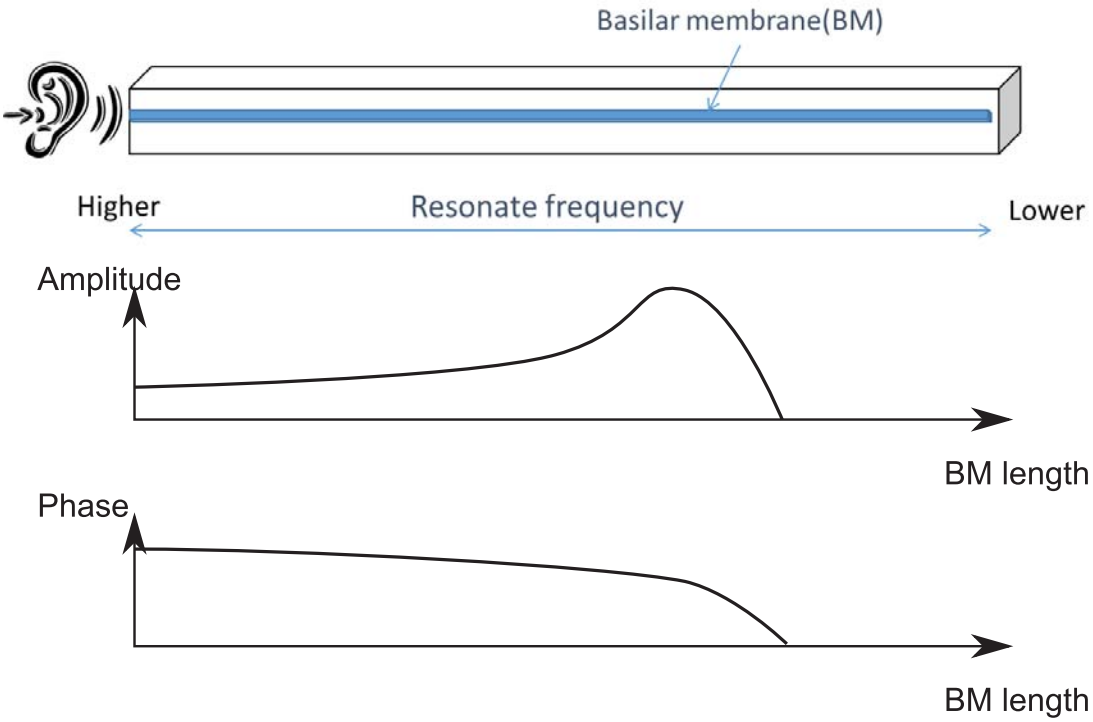

Figure 2.4: Schematic illustration of the uncoiled cochlear tube (top), amplitude and phase of BM vibration for a frequency (middle and bottom), respectively.

After reaching the peak, the BM traveling wave decays rapidly. The phase is delayed from the base to the apex, as shown in Fig. 2.4 (bottom).

Chapter 3

Active and nonlinear cochlear model

3.1 Introduction

This chapter proposes an active and nonlinear cochlear model that is a one-dimensional transmission line model with feedback from an active process. Previously, Neely and Kim proposed an active and linear transmission line model of the cochlea. Here, we expand this linear model into a nonlinear model. In Section 3.2, we propose an active transmission line model that is described by both mechanical and electroacoustic representation. In Section 3.3, we propose an OHC model as an active and nonlinear element in the transmission line model of the cochlea. In Section 3.4, we estimate parameter values to mimic the dynamics of the human cochlea. In Section 3.5, we introduce a numerical method to solve the model. In Section 3.6, we summarize this chapter.

3.2 Transmission line model

3.2.1 Mechanical representation

The transmission line simulates the driving of the BM traveling wave by fluid dynamics. In the one-dimensional transmission line model, the traveling wave propagates in the x-plane from the stapes to the helicotrema. P_d is the pressure difference between the upper and lower scales of a box divided into compartments by the cochlear BM. P_d drives the BM displacement ξ_b. The macromechanical equation of the transmission line model is

$$\frac{\partial^2 P_d(x,t)}{\partial x^2} = \frac{2\rho}{H}\frac{\partial^2 \xi_b(x,t)}{\partial t^2}, \tag{3.1}$$

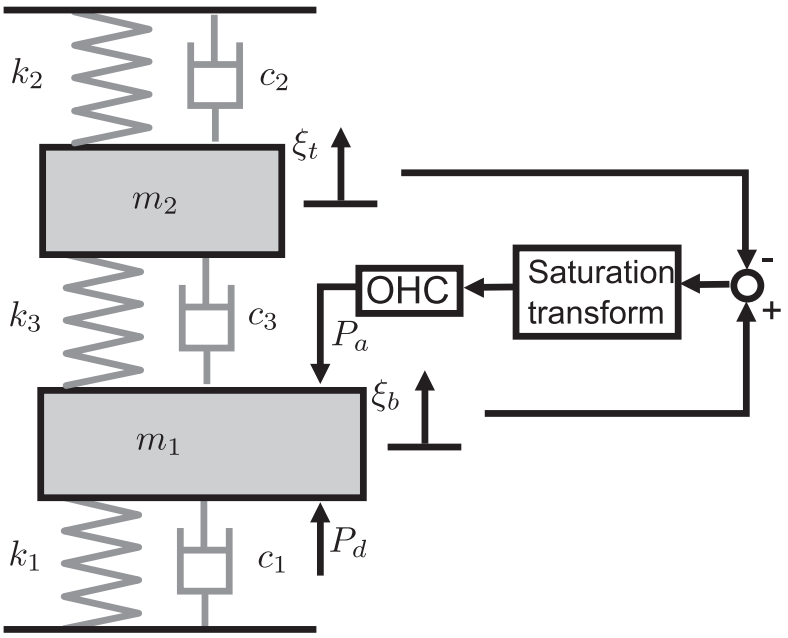

Figure 3.1: Micromechanical model of the cochlea

where ρ and H are the fluid density and scale width, respectively. The boundary conditions at the basal and apical ends of the cochlea are given by

$$\left.\frac{\partial P_d(x,t)}{\partial x}\right|_{x=0} = 2\rho\ddot{\xi}_s(t), \;\; P_d(x,t)|_{x=l} = 0 \tag{3.2}$$

where ξ_s represents the inward displacement of the stapes footplate, and the double-dot notation denotes the second time derivative.

To produce the sharp tuning observed in the cat's AN, the BM and TM were represented by the micromechanical model shown in Fig. 3.1. Denoting the pressure by $\mathbf{F}(x,t) = (P_d(x,t) - P_a(x,t), 0)^T$ and the displacement by $\xi(x,t) = (\xi_b(x,t), \xi_t(x,t))^T$, the equations of motion of the micromechanical model are given by

$$\mathbf{F} = \mathbf{M_p}\frac{\partial^2 \xi(x,t)}{\partial^2 t} + \mathbf{C_p}\frac{\partial \xi(x,t)}{\partial t} + \mathbf{K_p}\xi(x,t) \tag{3.3}$$

where

$$\mathbf{M_p} = \begin{pmatrix} m_1 & 0 \\ 0 & m_2 \end{pmatrix}, \; \mathbf{C_p} = \begin{pmatrix} c_1 + c_3 & -c_3 \\ -c_3 & c_2 + c_3 \end{pmatrix}, \; \mathbf{K_p} = \begin{pmatrix} k_1 + k_3 & -k_3 \\ -k_3 & k_2 + k_3 \end{pmatrix} \tag{3.4}$$

The initial conditions are given by

$$\xi(x,t)|_{t=0} = \mathbf{0}, \;\; \left.\frac{\partial \xi(x,t)}{\partial t}\right|_{t=0} = \mathbf{0}, \;\; \mathbf{P_a}(x,t) = 0. \tag{3.5}$$

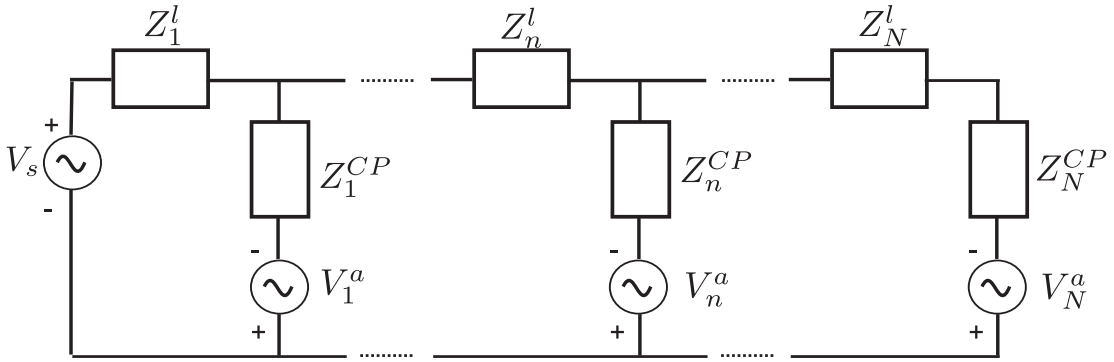

Figure 3.2: An electrical circuit of an active transmission line model of the cochlea.

The middle ear transmits the ear drum vibrations driven by sound pressure P_e to the cochlea. The middle ear is modeled as a one degree-of-freedom mass-spring-damper system with the following equation of motion:

$$P_e(t) = m_m \ddot{\xi}_s(t) + c_m \dot{\xi}_s(t) + k_m \xi_s(t), \tag{3.6}$$

where m_m, c_m, and k_m are the mass, damping, and stiffness, respectively, of the middle ear. The initial conditions are given by

$$\xi_s(0) = 0, \ \dot{\xi}_s(0) = 0. \tag{3.7}$$

3.2.2 Electroacoustic representation

The transmission line model of the cochlea can be represented by an electrical circuit. Figure 3.2 shows an electrical representation of the one-dimensional transmission line model using an electroacoustic analogy [43]. In this analogy, electrical voltage and current variables are analogous to pressure and volume velocity, and the electrical impedance of a circuit is equivalent to the acoustic impedance of a system.

In Fig. 3.2, a voltage source $V_s(t)$ drives the transmission line model, where $V_s(t)$ is analogous to the stapes sound pressure. The BM is spatially discretized into N segments. The present transmission line model expands the active linear model [30] to a nonlinear model. To produce the sharp tuning seen in the cat's AN, the micromechanical model was amplified using a voltage source $V_n^a(t)$ to represent the pressure generated by the OHC [30].

The electrical impedances Z_n^1, Z_n^2 and Z_n^3 represent the acoustic impedance of the BM, the TM and the hair bundles (HB), respectively. Inductance L, resistance R and capacitance C represent acoustical mass, resistance and compliance,

respectively

$$L = \frac{m}{b\Delta x}, R = \frac{c}{b\Delta x}, C = \frac{b\Delta x}{k}, \tag{3.8}$$

where m, c, and k are mass, damping, and stiffness per area, and b and Δx are the width of the BM and the segment length, respectively. The displacement of ξ_n at the nth segment is

$$\xi_n(t) = \frac{1}{b\Delta x} \int I_n(t) dt. \tag{3.9}$$

where $I_n(t)$ is the branch current at each segment.

The electrical impedance Z_n^l couples neighboring segments and represents the acoustic impedance of the fluid. The present transmission line model assumes that the fluid is lossless and not compressive. Inductance L_n^l represents the acoustic mass of fluid and is

$$L_n^l = \frac{2\rho\Delta x}{A}, \tag{3.10}$$

where ρ is the fluid density and A is the cross-sectional area of the scale.

In general, the circuit equation is defined as follows:

$$\boldsymbol{v}(t) = \boldsymbol{L}\dot{\boldsymbol{i}}(t) + \boldsymbol{R}\boldsymbol{i}(t) + \boldsymbol{S}\boldsymbol{q}(t), \tag{3.11}$$

where $\boldsymbol{v}$ is the voltage vector, $\boldsymbol{i}$ is the current vector, $\boldsymbol{q}$ is the electric charge vector, $\boldsymbol{L}$ is the inductance matrix, $\boldsymbol{R}$ is the resistance matrix and $\boldsymbol{S}$ is the compliance matrix (*i.e.,* the reciprocal of capacitance). Furthermore, a state space model is obtained from the above equation:

$$\begin{pmatrix} \dot{\boldsymbol{i}}(t) \\ \dot{\boldsymbol{q}}(t) \end{pmatrix} = \begin{pmatrix} \boldsymbol{L}^{-1}\boldsymbol{R} & \boldsymbol{L}^{-1}\boldsymbol{S} \\ \boldsymbol{I} & \boldsymbol{0} \end{pmatrix} \begin{pmatrix} \boldsymbol{i}(t) \\ \boldsymbol{q}(t) \end{pmatrix} + \begin{pmatrix} \boldsymbol{L}^{-1} & \boldsymbol{0} \end{pmatrix} \begin{pmatrix} \boldsymbol{V}(t) \\ \boldsymbol{0} \end{pmatrix}. \tag{3.12}$$

The state space model is useful for investigating properties of the transmission line model [44, 45].

To use mesh analysis [], the voltage $\boldsymbol{v}$, current $\boldsymbol{i}$ and electric charge vectors $\boldsymbol{q}$ in Fig. 3.3 are set by

$$\boldsymbol{V}(t) = \begin{pmatrix} V^s(t) + V_1^a(t) \\ V_2^a(t) - V_1^a(t) \\ \vdots \\ V_N^a(t) - V_{N-1}^a(t) \end{pmatrix}, \ \boldsymbol{i} = \begin{pmatrix} i_1^1(t) \\ i_1^3(t) \\ \vdots \\ i_N^1(t) \\ i_N^3(t) \end{pmatrix}, \ \boldsymbol{q} = \begin{pmatrix} q_1^1(t) \\ q_1^3(t) \\ \vdots \\ q_N^1(t) \\ q_N^3(t) \end{pmatrix}. \tag{3.13}$$

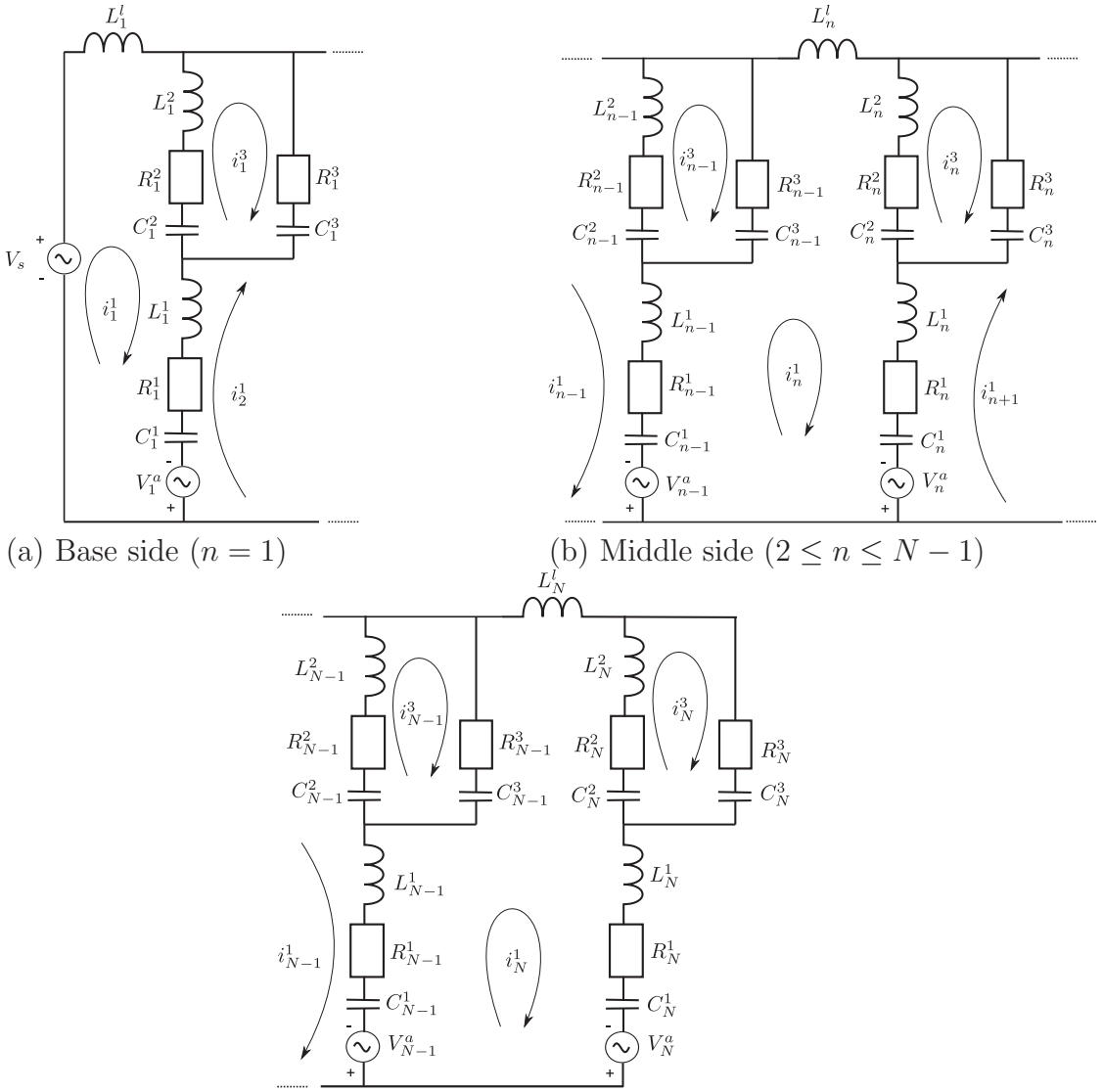

(a) Base side ($n = 1$)

(b) Middle side ($2 \leq n \leq N-1$)

(c) Apex side ($n = N$)

Figure 3.3: Electrical circuit representation of the Neely and Kim model proposed in Ref. [30]

The inductance $\boldsymbol{L}$, resistance $\boldsymbol{R}$ and compliance matrices $\boldsymbol{S}$ are

$$\begin{aligned}
\boldsymbol{L} &= \begin{pmatrix} \boldsymbol{I} \\ \boldsymbol{0} \end{pmatrix} \begin{pmatrix} \boldsymbol{L}_1^{CP} & \boldsymbol{0} \end{pmatrix} + \cdots + \begin{pmatrix} \boldsymbol{0} \\ \boldsymbol{I} \end{pmatrix} \begin{pmatrix} \boldsymbol{0} & \boldsymbol{L}_N^{CP} \end{pmatrix} \\
\boldsymbol{R} &= \begin{pmatrix} \boldsymbol{I} \\ \boldsymbol{0} \end{pmatrix} \begin{pmatrix} \boldsymbol{R}_1^{CP} & \boldsymbol{0} \end{pmatrix} + \cdots + \begin{pmatrix} \boldsymbol{0} \\ \boldsymbol{I} \end{pmatrix} \begin{pmatrix} \boldsymbol{0} & \boldsymbol{R}_N^{CP} \end{pmatrix} \\
\boldsymbol{S} &= \begin{pmatrix} \boldsymbol{I} \\ \boldsymbol{0} \end{pmatrix} \begin{pmatrix} \boldsymbol{S}_1^{CP} & \boldsymbol{0} \end{pmatrix} + \cdots + \begin{pmatrix} \boldsymbol{0} \\ \boldsymbol{I} \end{pmatrix} \begin{pmatrix} \boldsymbol{0} & \boldsymbol{S}_N^{CP} \end{pmatrix}
\end{aligned} \tag{3.14}$$

where $\boldsymbol{L}_n^{CP}$, $\boldsymbol{R}_n^{CP}$, and $\boldsymbol{S}_n^{CP}$ are the matrices of inductance, resistance, and compliance at each branch. On the base side ($n = 1$), the matrices $\boldsymbol{L}_1^{CP}$, $\boldsymbol{R}_1^{CP}$, and

$\boldsymbol{S}_1^{CP}$ are set by

$$\begin{aligned}
\boldsymbol{L}_1^{CP} &= \begin{pmatrix} L_1^l + L_1^1 + L_1^2 & -L_1^2 & -L_1^1 \\ -L_1^2 & L_1^2 + L_1^3 & -L_1^3 \end{pmatrix} \\
\boldsymbol{R}_1^{CP} &= \begin{pmatrix} R_1^1 + R_1^2 & -R_1^2 & -R_1^1 \\ -R_1^2 & R_1^2 + R_1^3 & -R_1^3 \end{pmatrix} \\
\boldsymbol{S}_1^{CP} &= \begin{pmatrix} \frac{1}{C_1^1} + \frac{1}{C_1^2} & -\frac{1}{C_1^2} & -\frac{1}{C_1^1} \\ -\frac{1}{C_1^2} & \frac{1}{C_1^2} + \frac{1}{C_1^3} & -\frac{1}{C_1^3} \end{pmatrix}.
\end{aligned} \tag{3.15}$$

On the middle side ($2 \leq n \leq N-1$), the matrices $\boldsymbol{L}_n^{CP}$, $\boldsymbol{R}_n^{CP}$, and $\boldsymbol{S}_n^{CP}$ are set by

$$\boldsymbol{L}_n^{CP} = \begin{pmatrix} -L_{n-1}^1 & -L_{n-1}^3 & L_{n-1}^1 + L_{n-1}^3 + L_n^l + L_n^1 + L_n^2 & -L_n^2 & -L_n^1 \\ -L_n^2 & 0 & -L_n^3 & L_n^2 + L_n^3 & 0 \end{pmatrix} \tag{3.16}$$

$$\boldsymbol{R}_n^{CP} = \begin{pmatrix} -R_{n-1}^1 & -R_{n-1}^3 & R_{n-1}^1 + R_{n-1}^3 + R_n^1 + R_n^2 & -R_n^2 & -R_n^1 \\ -R_n^2 & 0 & -R_n^3 & R_n^2 + R_n^3 & 0 \end{pmatrix} \tag{3.17}$$

$$\boldsymbol{S}_n^{CP} = \begin{pmatrix} -\frac{1}{C_{n\ 1}^1} & -\frac{1}{C_{n\ 1}^3} & \frac{1}{C_{n\ 1}^1} + \frac{1}{C_{n\ 1}^3} + \frac{1}{C_n^1} + \frac{1}{C_n^2} & -\frac{1}{C_n^2} & -\frac{1}{C_n^1} \\ -\frac{1}{C_n^2} & 0 & -\frac{1}{C_n^3} & \frac{1}{C_n^2} + \frac{1}{C_n^3} & 0 \end{pmatrix}. \tag{3.18}$$

On the apex side ($n = N$), the matrices $\boldsymbol{L}_N^{CP}$, $\boldsymbol{R}_N^{CP}$, and $\boldsymbol{S}_N^{CP}$ are

$$\begin{aligned}
\boldsymbol{L}_N^{CP} &= \begin{pmatrix} -L_{N-1}^1 & -L_{N-1}^3 & L_{N-1}^1 + L_{N-1}^3 + L_N^l + L_N^2 + L_N^1 & -L_N^2 \\ 0 & 0 & -L_N^2 & L_N^2 + L_N^3 \end{pmatrix} \\
\boldsymbol{R}_N^{CP} &= \begin{pmatrix} -R_{N-1}^1 & -R_{N-1}^3 & R_{N-1}^1 + R_{N-1}^3 + R_N^2 + R_N^1 & -R_N^2 \\ 0 & 0 & -R_N^2 & R_N^2 + R_N^3 \end{pmatrix} \\
\boldsymbol{S}_N^{CP} &= \begin{pmatrix} -\frac{1}{C_{N\ 1}^1} & -\frac{1}{C_{N\ 1}^2} & \frac{1}{C_{N\ 1}^1} + \frac{1}{C_{N\ 1}^3} + \frac{1}{C_N^2} + \frac{1}{C_N^1} & -\frac{1}{C_N^2} \\ 0 & 0 & -\frac{1}{C_N^2} & \frac{1}{C_N^2} + \frac{1}{C_N^3} \end{pmatrix}.
\end{aligned} \tag{3.19}$$

3.3 Outer hair cell model

The channel-opening probability of the hair cell mechanoelectric transducer $\mathrm{G_{tr}}(\xi_c(t))$ can be saturated by applying a second-order Boltzmann function, which relates the probability of a transducer channel opening to the displacement of a hair bundle ξ_c [46]:

$$\mathrm{G_{tr}}\left(\xi_c\left(t\right)\right) = \frac{1}{\left[1 + K_2\left(1 + K_1\right)\right]}, \tag{3.20}$$

where t denotes time and K_1 and K_2 are constants given by

$$\begin{aligned}
K_1 &= \exp\left[a_1\left(\xi_{c1} - \xi_c\left(t\right) + \xi_{c_rest}\right)\right] \\
K_2 &= \exp\left[a_2\left(\xi_{c2} - \xi_c\left(t\right) + \xi_{c_rest}\right)\right].
\end{aligned} \tag{3.21}$$

In (6), a_1, a_2, ξ_{c1}, and ξ_{c2} are constants, and ξ_{c_rest} is the rest point of the hair bundle.

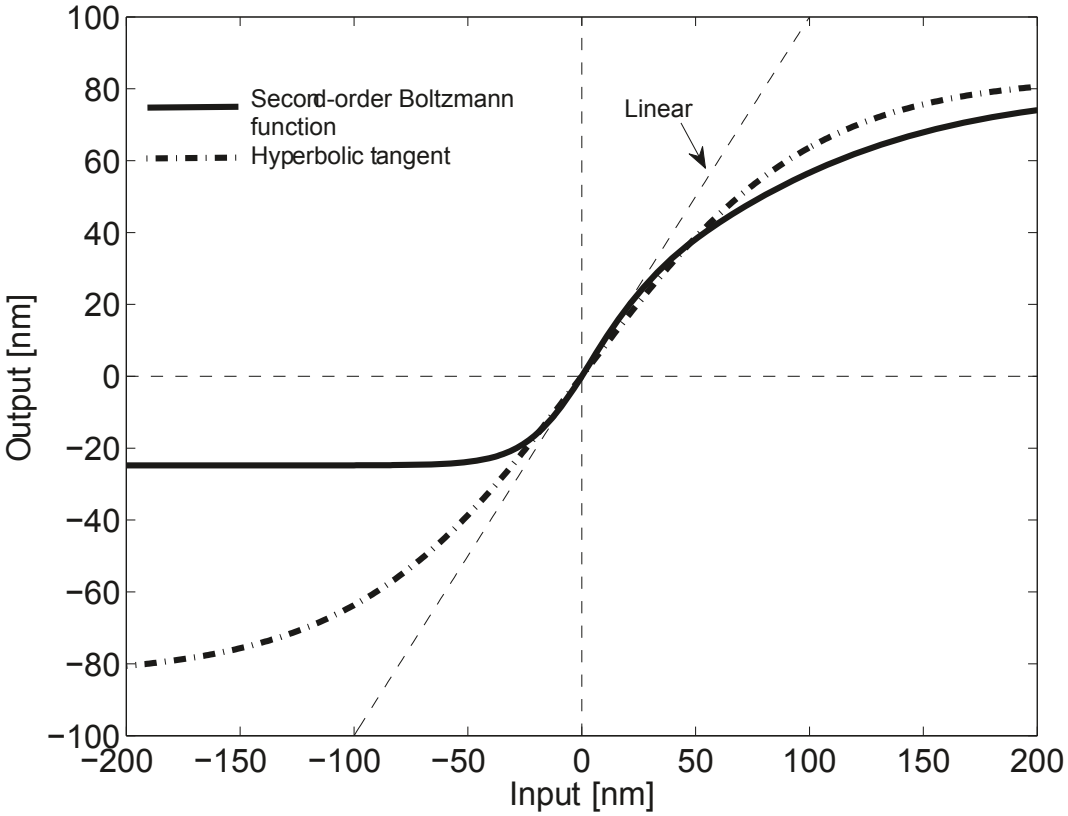

Figure 3.4: Electrical circuit of an active transmission line model of the cochlea.

Both the scale and offset of $\mathrm{G_{tr}}(\xi_c(t))$ are changed according to the following saturation function:

$$\xi_c^{nl}(t) = \alpha_{tr}\left[\mathrm{G_{tr}}\left(\xi_c(t) + \xi_{c\_rest}\right) - \mathrm{G_{tr}}\left(\xi_{c\_rest}\right)\right], \tag{3.22}$$

where ξ_{c_rest} is the rest point of the hair bundle and α_{tr} is chosen such that $\xi_c^{nl}(t) = \xi_c(t)$ when the amplitude of $\xi_c(t)$ is less than 1 nm. Figure 3.4 compares the IO property of Eq. (3.22) and the hyperbolic tangent function Eq. (5.1).

The OHC model senses the gap between the BM and TM and gives feedback to the BM, amplifying its motion. The gap is defined as the hair bundle displacement ξ_c, which depends on location and time:

$$\xi_c(x,t) = \xi_b(x,t) - \xi_t(x,t). \tag{3.23}$$

The amount of feedback P_a is

$$P_a(x,t) = \gamma\left(c_4\dot{\xi}_c^{nl}(x,t) + r_4\xi_c^{nl}(x,t)\right), \tag{3.24}$$

where c_4 and r_4 are the damping and stiffness coefficients, respectively, and ξ_c^{nl} is calculated by Eq. (3.22). For low displacements (< 1 nm), our model reduces to Neely and Kim's model, because ξ_c^{nl} equals ξ_c in Eq. (3.22).

3.4 Estimation of parameter values

The parameter values of the Neely–Kim model were fitted to the tuning curves of the cat AN. The cat values were modified to fit human data using the Greenwood function [47]. The quality factor of the BM was calculated as

$$Q_1 = \frac{\sqrt{m_1^{cat} k_1^{cat}}}{c_1^{cat}}, \tag{3.25}$$

where the superscript *cat* refers to the parameters of the Neely–Kim model, and

$$m_1 = m_1^{cat},\ c_1 \simeq m_1 \left(2\pi f_{human}(x)\right)^2, and\ k_1 \simeq \frac{\sqrt{m_1 k_1}}{Q_1}. \tag{3.26}$$

$f_{human}(x_n)$ is the human frequency–position map obtained from the Greenwood function. The damping and stiffness coefficients of the TM, HB, and OHC were assumed to be proportional to the ratio of the human and cat BM coefficients; that is

$$m_2 = m_2^{cat},\ c_i = c_i^{cat}\frac{c_1}{c_1^{cat}},\ k_i = 2k_i^{cat}\frac{k_1}{k_1^{cat}},\ i = \{2,\ 3,\ 4\}. \tag{3.27}$$

The parameter values are listed in Tables 3.1 and 3.2.

3.5 Numerical method

3.5.1 Mechanical model

The transmission line model is solved in the time domain in two steps. At each time step, the first and second steps solve the boundary value differential equation (Eq. 3.1) and the initial value differential equation (Eq. 3.3), respectively. The middle ear model (Eq. 3.6) is solved in the time domain given its initial condition (Eq. 3.7). We selected the finite difference method for the boundary value problem and the Runge–Kutta method for the initial value problem, noting that Runge–Kutta is the most common numerical method in the time domain Ref.[48]. The time-step Δt is $3\mu s$.

Table 3.1: List of parameters in the present cochlear model. The parameters in the middle ear model are taken from Ref. [30]. The parameter values were chosen to accord with the CFs of human cochleas in ref. [47].

Parameter	Value	Unit	Description
l	0.035	m	Total length of the BM
N	512		Number of spatial points in the x dimension
ρ	1000	$\mathrm{kg/m^3}$	Density of perilymph
A	10^{-6}	$\mathrm{m^2}$	Cross-sectional area of the cochlear scala
b	10^{-3}	m	Width of the BM
m_1	3×10^{-2}	$\mathrm{kg/m^2}$	BM mass per unit area
c_1	$60 + 6700e^{-150x}$	$\mathrm{N \cdot s/m^3}$	BM damping per unit area
k_1	$2.2 \times 10^8 e^{-300x}$	$\mathrm{N/m^3}$	BM stiffness per unit area
m_2	5×10^{-3}	$\mathrm{kg/m^2}$	TM mass per unit area
c_2	$44e^{-165x}$	$\mathrm{N \cdot s/m^3}$	TM damping per unit area
m_3	$1.4 \times 10^7 e^{-330x}$	$\mathrm{N/m^3}$	TM stiffness per unit area
c_3	$8e^{-60x}$	$\mathrm{N \cdot s/m^3}$	Resistance of the OHC's HB per unit area
s_3	$2 \times 10^6 e^{-3x}$	$\mathrm{N/m^3}$	Stiffness of the OHC's HB per unit area
c_4	$4400e^{-150x}$	$\mathrm{N \cdot s/m^3}$	Resistance driven by OHC's motility per unit area
k_4	$1.15 \times 10^9 e^{-300x}$	$\mathrm{N/m^3}$	Stiffness driven by OHC's motility per unit area
γ	1		Gain factor

Table 3.2: List of parameters in the OHC mechanoelectric transducer function, obtained from Ref. [46].

Parameter	Value	Unit	Description
ξ_{c_rest}	2.0×10^{-8}	m	Resting displacement of the OHC's HB
α_{tr}	1.04×10^{-7}	m	Maximum displacement of nonlinear transduction
a_1	65×10^6	$\mathrm{m^{-1}}$	Constant for K_1 in Eq. (7)
a_2	16×10^6	$\mathrm{m^{-1}}$	Constant for K_2 in Eq. (7)
x_1	24×10^{-9}	m	Constant for K_1 in Eq. (7)
x_2	41×10^{-9}	m	Constant for K_2 in Eq. (7)

To solve the boundary value differential equation (Eq. 3.1), we rewrite the equation by substituting Eq 3.3 in Eq. 3.1, which yields

$$\frac{\partial^2 P_d(x,t)}{\partial x^2} - \Omega(x) P_a(x,t) = g(x,t)\Omega(x), \tag{3.28}$$

where

$$\Omega(x) = \frac{2\rho}{m_1 H}, \tag{3.29}$$

$$g(x,t) = -\left(c_1(x)\frac{\partial \xi_b(x,t)}{\partial t} + k_1(x)\xi_b(x,t) + P_a(x,t)\right). \tag{3.30}$$

Let us define the pressure difference vector $\boldsymbol{P_d}$:

$$\boldsymbol{P_d}(t) = \left[P_1^d(t) \cdots P_N^d(t)\right]^T, \tag{3.31}$$

where $P_n^d(t) = P_d(x_n, t)$. Applying a linear combination of the Taylor expansions for P_{n-1} and P_{n+1} yields

$$\left.\frac{\partial^2 P_d(x,t)}{\partial x^2}\right|_{x=x_n} = \frac{P_{n-1}^d(t) - 2P_n^d(t) + P_{n+1}^d(t)}{\Delta x^2} + \mathcal{O}(h^2),\ 2 \le n \le N - \tag{3.32}$$

$$\left.\frac{\partial^2 P_d(x,t)}{\partial x^2}\right|_{x=0} = \frac{2\left(P_2^d(t) - P_1^d(t) - \Delta x \dot{P}_1^d(t)\right)}{\Delta x^2} + \mathcal{O}(h), \tag{3.33}$$

where $\dot{P}_1^d(t) = 2\rho\dot{\xi}_s(t)$ is derived from the boundary values (Eq. 3.2). Because we assume that P is a smooth function, the boundary-value problem (Eq. 3.28) can be expressed as a set of linear equations:

$$\boldsymbol{\Delta P_d} = \boldsymbol{Y}, \tag{3.34}$$

where

$$\boldsymbol{Y} = \begin{pmatrix} 2h\rho\xi_s'(t) + \frac{1}{2}\Delta x^2 g(x_0,t)\Omega(x_0) \\ h^2 g(x_1,t)\Omega(x_1) \\ \vdots \\ h^2 g(x_{N-1},t)\Omega(x_{N-1}) \\ 0 \end{pmatrix}, \tag{3.35}$$

and

$$\Delta = \begin{pmatrix} -\left(1 + \frac{\Delta x^2 \Omega(x_0)}{2}\right) & 1 & 0 & & \cdots 0 & \\ 1 & -(2 + \Delta x^2 \Omega(x_1)) & 1 & 0 & \cdots & 0 \\ & \ddots & \ddots & \ddots & & \\ 0 & \cdots & 0 & 1 & -(2 + \Delta x^2 \Omega(x_{N-1})) & 1 \\ 0 & \cdots & & & 0 & 1 \end{pmatrix}. \tag{3.36}$$

In the second step, the initial value differential equation (Eq. 3.3) is solved using the Runge–Kutta method. Let us define the state vector $\boldsymbol{x}$ and the input vector $\boldsymbol{u}$.

$$\boldsymbol{x}(t) = \left(\dot{\boldsymbol{\xi}}_1(t) \cdots \dot{\boldsymbol{\xi}}_N(t) \boldsymbol{\xi}_1(t) \cdots \boldsymbol{\xi}_N(t)\right)^T, \boldsymbol{u}(t) = (\boldsymbol{F}(t), 0 \cdots 0)^T \tag{3.37}$$

where $\boldsymbol{\xi}_n(t) = \boldsymbol{\xi}(x_n, t)$. We rewrite Eq. 3.3 into first order differential equations:

$$\begin{aligned} \dot{\boldsymbol{x}}(t) &= f\left(t, \boldsymbol{x}, \boldsymbol{u}\right) \\ &= \begin{pmatrix} \boldsymbol{M}_P^{-1}\boldsymbol{C}_P & -\boldsymbol{M}_P^{-1}\boldsymbol{K}_P \\ \boldsymbol{I} & \boldsymbol{0} \end{pmatrix} \boldsymbol{x}(t) + \boldsymbol{u}(t). \end{aligned} \tag{3.38}$$

The equation is solved by the Runge–Kutta method that is widely used in the cochlear initial value problem [48]. This method calculates the state vector $\boldsymbol{x}(t)$ in Eq. 3.38 at any time t with time step Δt.

$$\begin{aligned} k_1 &= \Delta t \cdot f\left(t, \boldsymbol{x}_n, \boldsymbol{y}_t\right) \\ k_2 &= \Delta t \cdot f\left(t + \frac{\Delta t}{2}, \boldsymbol{x}_n + \frac{\Delta t}{2}, \boldsymbol{y}_n + \frac{k_1}{2}\right) \\ k_3 &= \Delta t \cdot f\left(t + \frac{\Delta t}{2}, \boldsymbol{x}_n + \frac{\Delta t}{2}, \boldsymbol{y}_n + \frac{k_2}{2}\right) \\ \boldsymbol{x}_{n+1} &= \boldsymbol{x}_n + \Delta t \\ k_4 &= \Delta t \cdot f\left(t + \Delta t, \boldsymbol{x}_{n+1}, \boldsymbol{y}_n + k_3\right) \\ \boldsymbol{y}_{n+1} &= \boldsymbol{y}_n + \frac{k_1 + 2k_2 + 2k_3 + k_4}{6} \end{aligned} \tag{3.39}$$

3.5.2 Electroacoustic model

The electroacoustic representation in the cochlear transmission line model shows the first order differential equation (Eq. 3.13). This form can be solved using the Runge–Kutta method (Eq. 3.39).

3.6 Example of output and stability of transmission line model solved by linear solution

In this section, we show examples of outputs and the stability of the transmission line model in solving the cochlear equation (Eq. 3.12) in the linear domain.

Figure 3.5 shows BM velocity and phase along the cochlear length with parameter values set to those in the original Neely and Kim model. The peak of the amplitude of the BM velocity depends on the sound frequency. The amplitude of

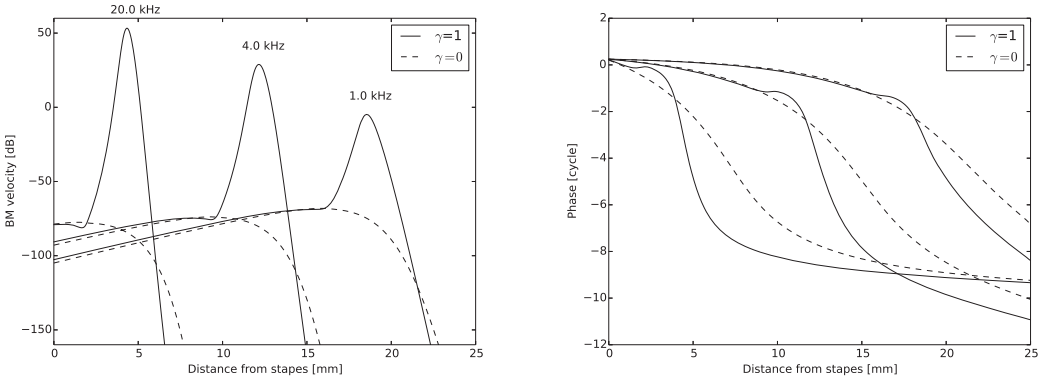

Figure 3.5: BM velocity and phase response in the linear domain

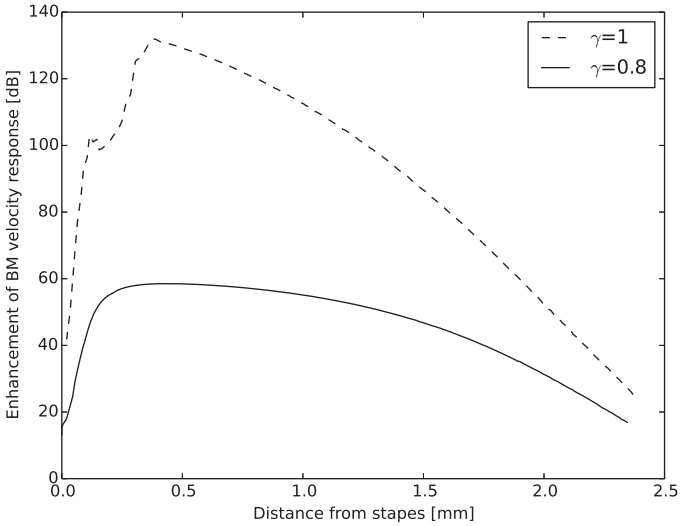

Figure 3.6: BM velocity and phase response calculated in the linear domain

the BM velocity is amplified by the OHC model, where the gain factor $\gamma = 1$. The phase of the BM velocity is delayed from base to apex.

Figure 3.5 shows the amount of enhancement of BM velocity along the cochlear length. For the original gain factor, $\gamma = 1$, the enhancement is over 100 dB at the base side. For the lower gain factor, $\gamma = 0.8$, the enhancement is about 50 dB.

The transfer function of the transmission line model described in an electroacoustic way (Eq. 3.12) is

$$\mathrm{G}(s) = (s\boldsymbol{I} - \boldsymbol{A})^{-1}\boldsymbol{B}, \tag{3.40}$$

where

$$\boldsymbol{A} = \begin{pmatrix} \boldsymbol{L}^{-1}\boldsymbol{R} & \boldsymbol{L}^{-1}\boldsymbol{S} \\ \boldsymbol{I} & \boldsymbol{0} \end{pmatrix} \boldsymbol{B} = \begin{pmatrix} \boldsymbol{L}^{-1} & \boldsymbol{0} \end{pmatrix}. \tag{3.41}$$

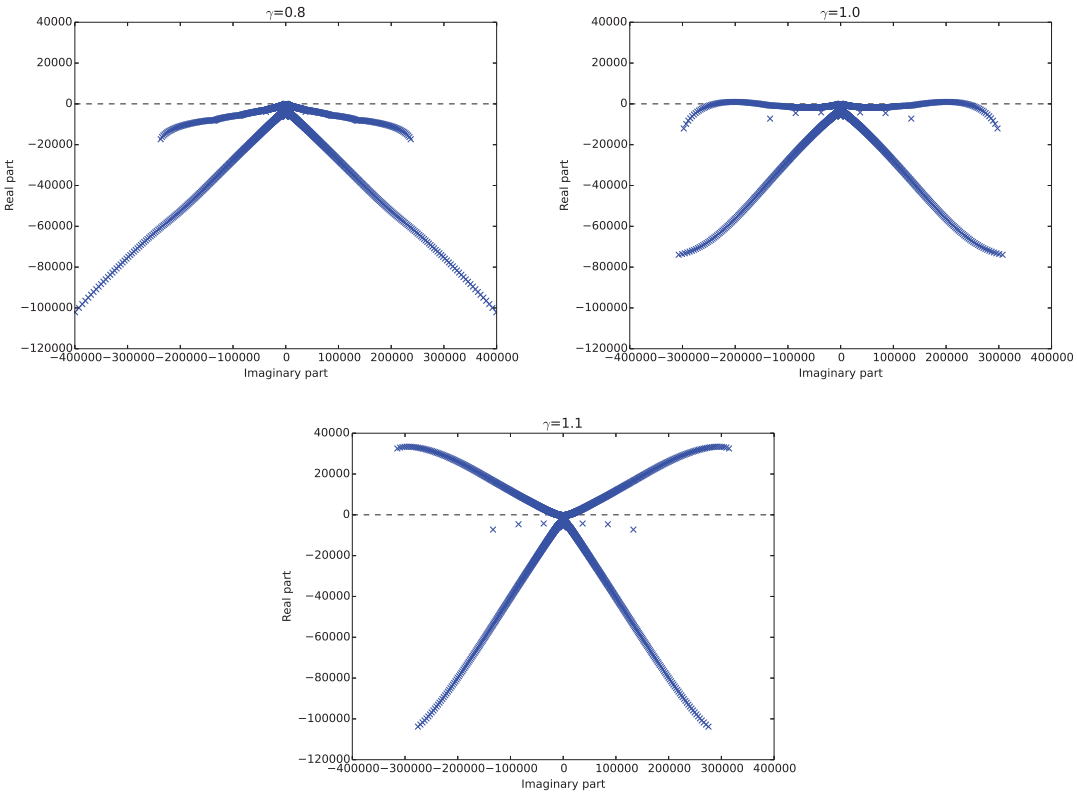

Figure 3.7: Poles of the active and linear cochlear model

To evaluate the stability of the transmission line model, we calculate the poles of the transfer function G(s) shown in Fig. 3.7. For a lower gain factor of $\gamma = 0.8$, the real parts of the poles show negative values. For a gain factor of $\gamma = 1.0$, the locations of the real parts of the poles are around zero. For a higher gain factor of $\gamma = 1.1$, the positive real parts of the poles are obtained. These results suggest that the cochlear model is stable when the gain factor γ is less than one.

3.7 Summary

This chapter introduced the active and nonlinear transmission line model of the cochlea. This model contains saturating feedback that is modeled by the OHC activity, and is equal to the Neely and Kim model [30] when BM displacement is at a lower level. The transmission line model can be described by both mechanical and electroacoustic representations. Both representations are spatially discretized into segments and solved using a time domain solution. The parameter values were fitted to the human cochlear frequency map.

Chapter 4

Compression

4.1 Introduction

Recently, psychological methods have been proposed to estimate nonlinear cochlear input - output (IO) functions [15, 49]. In particular, the nonlinear slope of the cochlear function, around 0.2 dB/dB, at a moderate input level is called compression [14]. It is difficult to determine the physiological mechanisms of the psychologically estimated cochlear IO function. Model studies can fill a gap in findings between psychological studies and physiological studies. A phenomenological model has been used to point out a simple nonlinear function producing compression [50]. However, the phenomenological model only focuses on the relationship between the input and output and regards the system as a black box [51]. To understand mechanisms of the psychologically estimated cochlear IO function, a physiological cochlear model is needed. The physiological cochlear model proposed in the Ch. 3 is tested. However, there is a problem that the simulation paradigm differ to compare the data obtained from simultaneous masking. Simultaneous masking means suppressing a tone with other tone. To estimate the cochlear IO function, a masking is needed under the condition of no suppression.

We determines the physiological mechanisms of the psychologically estimated cochlear IO function. To make conditions of no suppressing a signal with a maker, pulsation threshold as non simultaneous masking is employed. In this case, a signal and masker do not overlap temporally. We simulates the pulsation threshold using a physiological cochlear model and estimates cochlear IO functions. Estimated cochlear IO functions obtained from the simulation are compared both qualitatively and quantitatively. Finally, we discuss a relationship between the psychologically estimated cochlear IO function and physiological functions of the

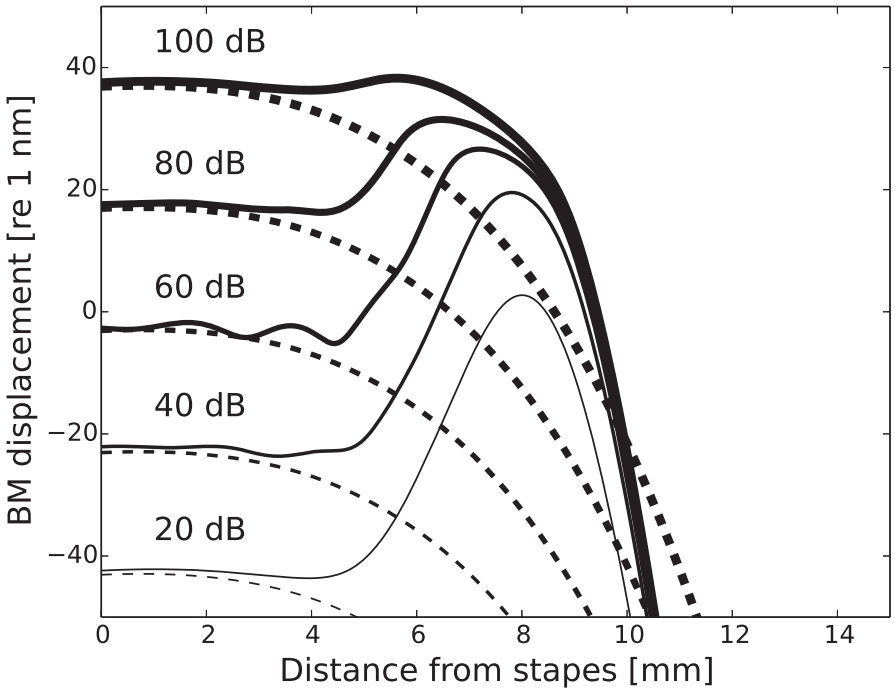

Figure 4.1: Spatial BM responses for pure tones. The sound pressure level is varied from 20 to 100 dB in 20 dB steps. The frequency is 6000 Hz. Solid and dashed lines plot responses of the complete model and the model excluding OHCs, respectively

cochlea.

4.2 Comparison with physiological measurements

4.2.1 Method

The transmission line model of the cochlea is used to simulate single tone BM responses. The frequencies f_p of the probe tone were varied from 1000 – 9000 Hz in 100 Hz steps. The intensities L_p were increased from 0 to 100 dB in 10 dB steps. The tone was presented for 55 ms, with rise/fall times of 5 ms. The model outputs were recored for 10 ms, starting 40 ms after tone presentation.

4.2.2 Result

Figure 4.1 shows the amplitude of BM displacement excited by a single tone as a function of the cochlear length. OHCs amplified BM motion around $x = 7.9$ mm from the base. Each gain of the amplification depends on the sound pressure level. For lower sound pressure level, the gain is over 50 dB. On the other hand, the gain

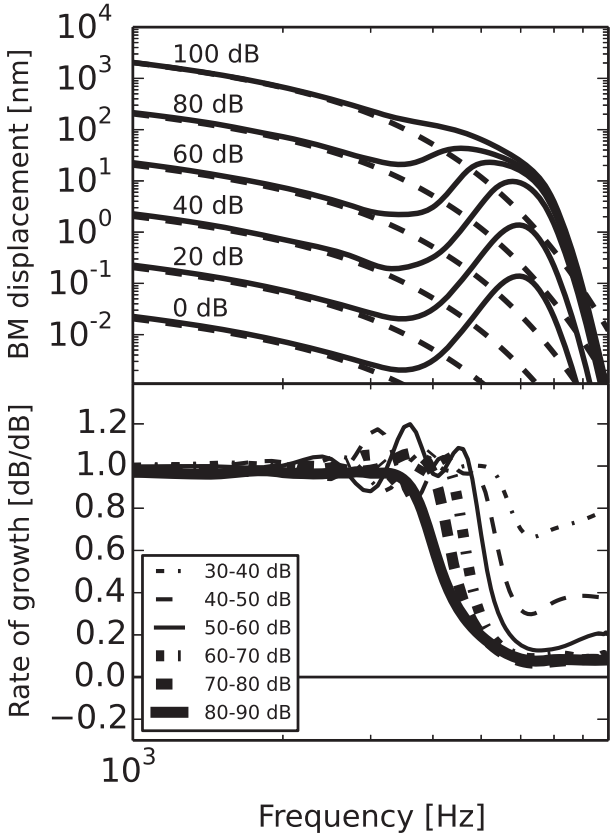

Figure 4.2: (Top) Iso-intensity functions (frequency responses) at CF = 6000 Hz. The sound pressure is varied from 0 to 100 dB in 20 dB steps and the imposed frequency is varied from 1000 to 8000 Hz. Solid and dashed lines plot the frequency responses of the complete model and the model excluding OHCs, respectively. (Bottom) Rate of growth (ROG) functions (degree of compression) obtained from the slopes of the frequency response curves. Linear and perfectively compressive growth occur when ROG = 1 dB/dB and ROG = 0 dB/dB, respectively.

is less than 10 dB for higher sound pressure level.

Figure 4.2 (top) shows the amplitude of BM displacement at the CF as a function of the frequencies and levels of a single imposed tone, with and without OHC involvement. In these plots the CF is 6000 Hz, located at $x = 7.9$ mm from the base. Notice that the frequency response curves are sharper at lower input levels. The peak sharpness is characterized by the quality factor Q_{10} (CF/bandwidth measured at 10 dB below the peak). Q_{10} was 4.4 at 0 dB, comparable to animal experimental data ([52]). The frequency responses broadened and the gain was reduced as the input intensity increased. At frequencies lower than half an octave below the CF, the OHC process exerted little effect on the BM displacement. At around the CF, however, the OHCs amplified the BM displacement by over 50 dB,

relative to the case of no OHC involvement.

To characterize the degree of compression in the frequency response curve, the rate of growth (ROG) was plotted at various stimulus levels. The results are shown in the bottom panel of Fig. 6. At frequencies less than half an octave below the CF, the ROGs closely approximate 1 dB/dB. The ROGs around the CF are much less than 1 dB/dB (around 0.10 dB/dB), indicating a compressive nonlinearity around the CF.

4.2.3 Discussion

The BM responses to a pure tone were found to depend on input level (Figs. 4.1 and 4.2). Those results are realistic, because it implies that compression is solely caused by the attenuated cochlear amplification, itself imposed by the saturating properties of the OHCs. According to the OHC model described by Eq. (7), the output of the OHCs is linear at low displacement levels and saturates at higher levels, consistent with compression [14].

4.3 Comparison with psychological measurements

4.3.1 Method

Pulsation threshold

To estimate the cochlear IO function, the pulsation threshold technique is used [15]. Figure 4.3 shows the stimuli, signal and masker. The signal and masker are alternatively presented. The pulsation threshold is the threshold for the perception of the stimuli changing from continuous to pulsating or from pulsating to continuous. This perceptional phenomena could be accounted that amounts of the basilar membrane responses are same for both the signal and masker [53].

Simulation

A computational method to estimate the pulsation threshold has already been proposed [50]. Employing this method, the cochlear IO function is defined by the estimated masker level of threshold $\hat{L}_m$ as a function of signal level L_p. Figure 4.4(A) outlines the computational method, which comprises (1) a cochlear model and (2) estimation of the masker level threshold. In Ref. [50], a functional model of the cochlea [39] was used. The transmission line model of the cochlea is used to

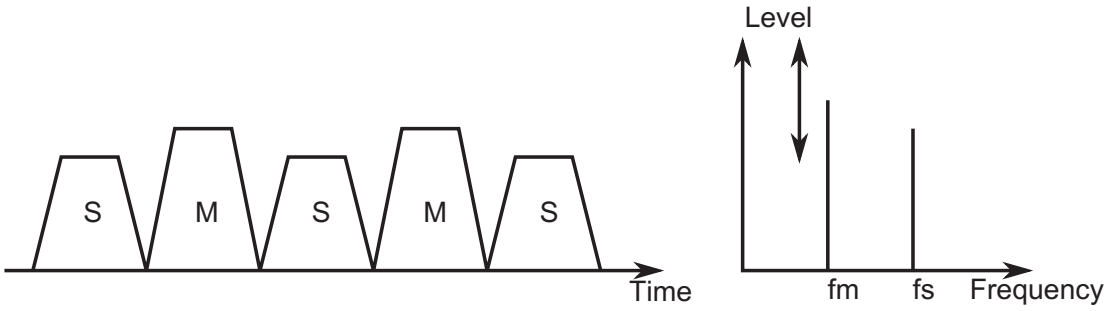

Figure 4.3: Schematic illustration of the temporal (left) and spectral (right) characteristics of the stimuli in the pulsation threshold technique. Symbols "S" and "M" are indicate the signal and the masker, respectively.

investigate the relationship between psychological measurements and physiological mechanisms.

First, two pure tones constructed by the signal and the masker are input to the cochlear model at different times. Signal frequency f_p is set to 250, 500, 1000, 2000, 4000 and 8000 Hz. Masker frequency f_s is set to $0.6f_p$. Outputs of the cochlear model are velocities of a basilar membrane (BM) model at the characteristic frequency, the most responsible location for the signal, equal to the signal frequency .

Finally, the masker level of the threshold is calculated from the simulation result of the cochlear model. Inputs of the estimating method are BM velocities for the signal and masker. If the BM velocity for the masker equals the BM velocity for the signal, then the output of the method is the estimated masker level of threshold $\hat{L}_m$. Otherwise, the workflow returns to the cochlear model and the BM velocity is calculated for the different masker level.

Figure 4.4 (B) is a block diagram of the transmission line model of the cochlea. The signal and masker as inputs of the cochlear model do not overlap temporally. Outputs of the cochlear model are the velocity of the BM. In the cochlear model, there is a feedback system to amplify the BM motion. However, the output of the feedback system could saturate with an increasing input level. The saturation property is derived from the outer hair cell (OHC) model. The OHC model is based on findings of the activity of the OHC and is constructed from the two elements shown at the bottom of Fig. 4.4 (B). The first element is modeled by mechanoelectrical transduction described in Ref. [46]. The second element is modeled by a springdamper system as the soma of the OHC.

Figure 4.4 (C) illustrates the method for estimating the threshold of the masker

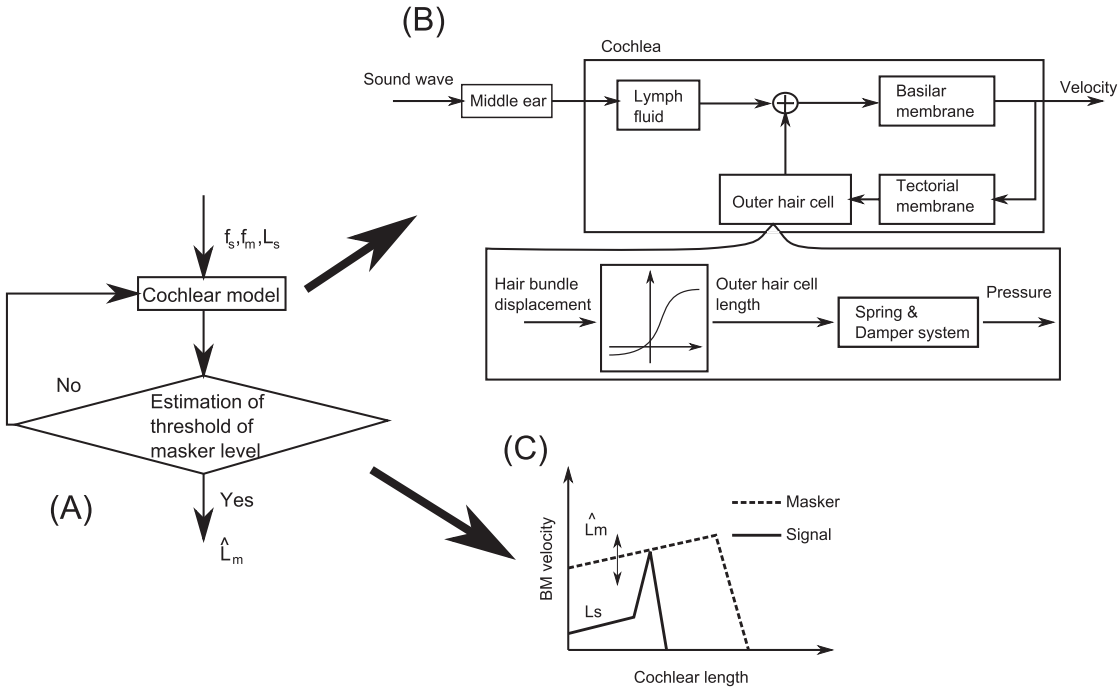

Figure 4.4: (A) Outline of the simulation. f_s: signal frequency. f_m: masker frequency. L_s: signal level. $\hat{L_m}$: Estimated masker level of the threshold. (B) Block diagram of the transmission line model of the cochlea. (C) Schematic illustration of outputs of the BM model and estimation of the threshold of the masker level . The masker level was set to fit a maximum response of the BM to the signal and a response of the BM for the masker at the same location

level. The pulsation threshold is described in Sec. 2.1. The threshold of the masker level is estimated as follows. (1) BM velocity ξ_s for the signal is calculated at the characteristic frequency ($=f_p$). (2) BM velocity ξ_m for the masker is calculated at the same location. (3) If the BM velocity for the masker ξ_m equals the BM velocity for the signal ξ_s, then the output of the method is the estimated masker level of threshold $\hat{L}_m$. Otherwise, the workflow returns to (2) and the BM velocity is calculated for the different masker level.

4.3.2 Result

Cochlear input-output function

Figure 4.5 shows cochlear IO functions estimated in the simulations. The rapid growth depends on the decreasing signal frequency below a frequency of 1000 Hz. At signal frequencies exceeding 1000 Hz, a break point appears at input levels of 40 to 50 dB. Afterward, the slopes are gentle. On the other hand, at signal

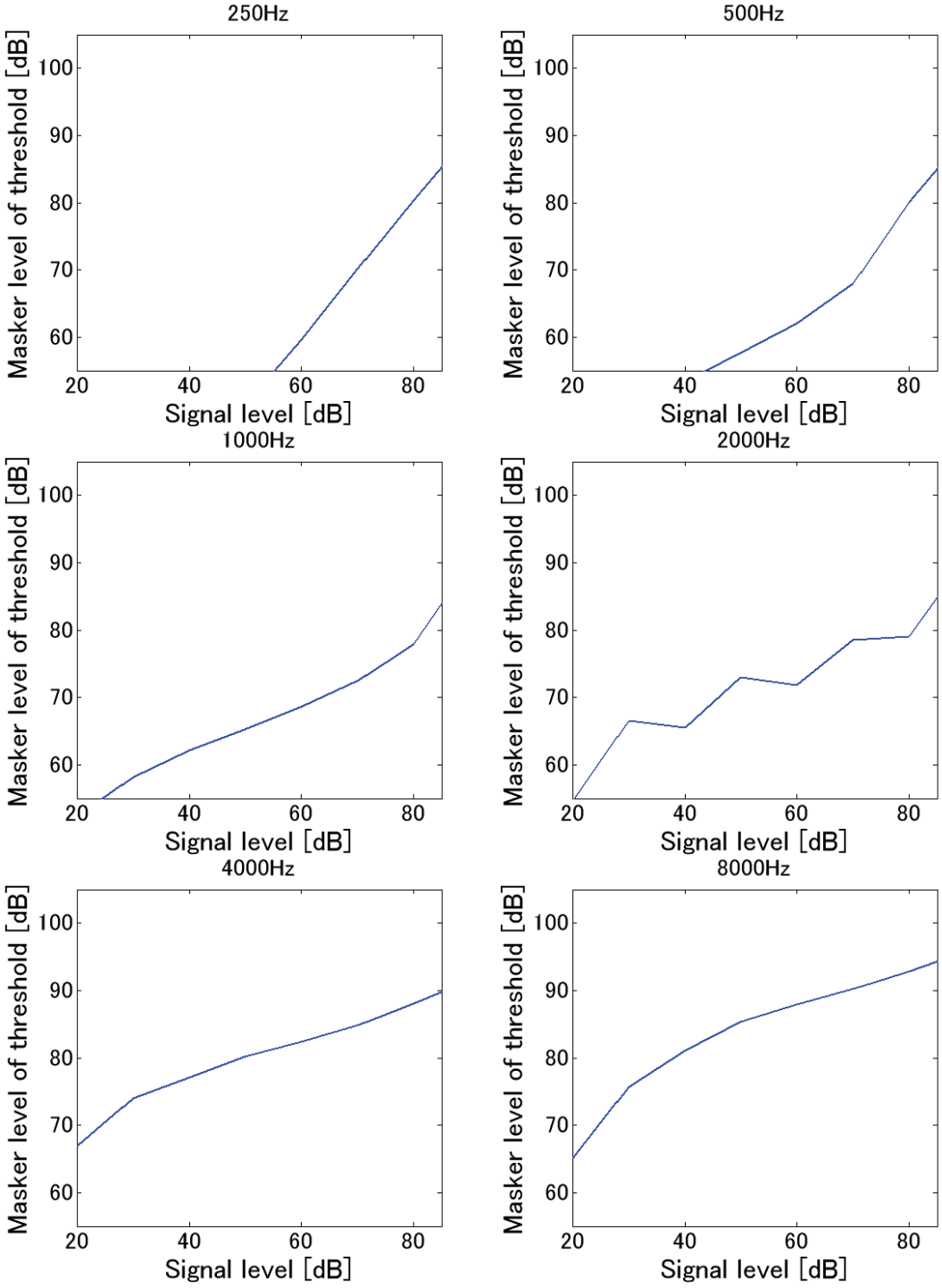

Figure 4.5: Cochlear IO functions estimated in the simulations. The signal frequency f_p is given above each figure.

frequencies of 500 and 1000 Hz, a break point appears at a higher input level. There is only one break point without a condition in the signal frequency of 1000 Hz .

Table 4.1: Slopes of the cochlear IO functions at moderate input levels (50 to 80 dB) [dB/dB] indicating the rate of the compression.

Signal frequency [Hz]	250	500	1000	2000	4000	8000
Plack and Oxenham. (2000) [dB/dB] [15]	0.76	0.50	0.34	0.32	0.33	0.41
Present study [dB/dB]	1.01	0.75	0.42	0.20	0.26	0.25

Rate of compression

To compare the rate of compression between the psychological result[15] and the simulation result, Table 4.1 presents the slopes of the cochlear IO functions at a moderate input level. The trend of the slopes obtained in the simulations is comparable to that in the experiments or is higher in the experiments. The rates of compression are higher and constant at signal frequencies exceeding 1000 Hz. At a signal frequency below 1000 Hz, the rate of compression decreases with signal frequency. In the physiological experiments [14], the slope is around 0.2 dB/dB at higher frequencies. The simulation results account for the results of physiological experiments.

4.3.3 Discussion

We sought to clarify the relationship between the physiological cochlear IO function and the psychological cochlear IO function. The physiological cochlear IO function is the maximum cochlear response as a function of the input level. The output of the psychological cochlear IO function differs apparently from the physiological cochlear IO function and is the threshold of the masker level as a function of the signal level. However, the results are compatible according to the hypothesis of the pulsation threshold. The model results showed that the growths of the cochlear responses were (1) compressive at the characteristic frequency and (2) linear at low frequency. Thus, the growths of the BM responses are compressive for the signal and linear for the masker.

The cochlear IO functions shown in Fig. 4.5 were obtained from the simulation. The shapes of the IO functions depending on the signal frequencies were compressive and similar to those obtained in the psychological experiment [15]. In the cochlear model, the nonlinear element is the OHC model and it produces the compression in the cochlear IO function. The OHC model is based on modeling the nonlinear motility of the OHC. Therefore, it is suggested that the motility of

the OHC produces the nonlinear cochlear IO function obtained from the pulsation threshold.

The ideal cochlear IO function has been proposed; the function has (1) linear growth at a lower input level, (2) compressive growth at a moderate input level and (3) linear growth at a higher input level [14]. There are two break points in the ideal cochlear IO function. Simulation results show one break point at lower or higher input levels except at signal frequency of 1000 Hz. This result is derived from the narrow range of input levels from 20 to 80 dB. Hence, the ideal cochlear IO function is simulated for the audible range from 0 to 120 dB .

Table 4.1 shows comparable rates of compression in the psychological [15] and physiological experiments . The results indicate that the simulations of the pulsation threshold not affected by suppression can be used to correct the nonlinear cochlear IO function . The results of the simultaneous masking experiments [54] show a rate of compression higher than the pulsation threshold. In simultaneous masking, the cochlear IO function is affected by suppression.

The shapes and rates of the cochlear IO functions obtained in the simulations depend on the signal frequency. These trends are due to BM amplification depending on the characteristic frequency. At the apex of the cochlea (having a lower characteristic frequency), the level of amplification is not great[52]. At the base of the cochlea (having a higher characteristic frequency), the level of amplification is great [52]. It has been suggested that the shapes and rates of the cochlear IO functions depend on the amplification generated by the activity of the OHC. The results of this simulation confirm this hypothesis.

4.4 Summary

In this chapter, we investigate how compression in the cochlear IO function is occurred using the transmission line model including the active and nonlinear OHC model. The OHC model is inspired from the OHC motilities and its IO function is fitted by the second order Botlzmann function as the saturation function. The results obtained from the model can account for both physiological and psychological measurements, and is caused by the active and nonlinear OHC model. This finding suggest mechanisms of compression in two steps. Firstly, at lower sound pressure level, the OHC model boots the BM motion linearly. Secondly, over moderate sound pressure level, this BM amplification is saturated in the OHC model.

Chapter 5

Two-tone suppression

5.1 Introduction

A distinctive feature of cochlear nonlinearity is two-tone suppression (2TS), in which one pure tone reduces the cochlear response to a second tone. The dominant and suppressed tones are called the suppressor and probe, respectively. This 2TS phenomenon, first observed in the auditory nerve (AN) half a century ago [16], has also been detected in the basilar membrane (BM) [17] and the inner hair cells (IHCs) [18] within the past two decades. Ref. [17] concluded that 2TS originates from mechanical phenomena at the BM and is generated by an active process. Some form of saturation is involved, as evidenced by the features of cochlear nonlinearity such as compression and distortion products. Compression can be realized by amplifying the saturation function (*e.g.* [14]), and distortion products are generated when two tones pass through the saturation process as inter modulation [55].

According to experimental measurements of mechanoelectric transduction by outer hair cells (OHCs), the saturation function can be described by a second-order Boltzmann function. This function purportedly explains the nonlinearities in cochlear mechanics [56]. The cochlear mechanism of Geisler and Nuttall [57] is based on a saturating function of 2TS imposed by a low-frequency suppressor on the BM. The low-frequency suppressor operates a rest point on the input-output (IO) property of the saturating function. However, the high-frequency tone suppresses the BM response of the probe in experiments ([58], [59]). Therefore, it appears that 2TS mechanisms are distinguishable by the frequency ratio of the 2TS.

Modeling studies can potentially explore 2TS mechanisms beyond the reach

of current experiments. Cochlear models can be classified into phenomenological models and transmission line models. Phenomenological models focus on the cochlear I/O properties, and fit the experimental 2TS data by simple nonlinear I/O functions [39, 40]. Transmission line models simulate the traveling wave dynamics of the cochlea. Neely and Kim suggested that sharp tuning can be realized by applying pressure to an active element on the BM [30]. Other workers have simulated 2TS using active elements that respond nonlinearly to sound pressure levels [34] or BM motions [36].

The present paper proposes a special saturation function that uniquely processes the combined input of two tones. This saturation function, which includes active and nonlinear elements, successfully generates 2TS on the BM. By incorporating this function into a nonlinear transmission line model, we conceptualize a novel 2TS mechanism.

5.2 Two-tone suppression in saturation function

5.2.1 Point operation theory

In the 2TS mechanism proposed by Geisler and Nuttall, the saturating function is based on a point operation [57]. The point operation for suppression is schematized in Fig. 1. Panels (a) and (b) of this figure display the I/O property of the saturating function and the output waveform, respectively. The input waveform is shown in Fig. 1c.

The output waveform is conserved when a low-level tone is input (dashed line in Fig. 1c), but is compressed when the input is a high-level tone in the nonlinear region.

Two-tone suppression in the saturating function arises by several mechanisms. First, a pair of tones with very different frequencies is input to the saturating function as shown in Fig. 1c. Second, the peaks of the output waveform are greatly compressed (Fig. 1b). Finally, the effects of the lower frequency tone are removed by passing the output waveform through a high-pass filter (Fig. 1d). The suppressive and temporal features of the filtered wave arise because the lower frequency tone governs the rest point of the higher frequency tone on the IO property.

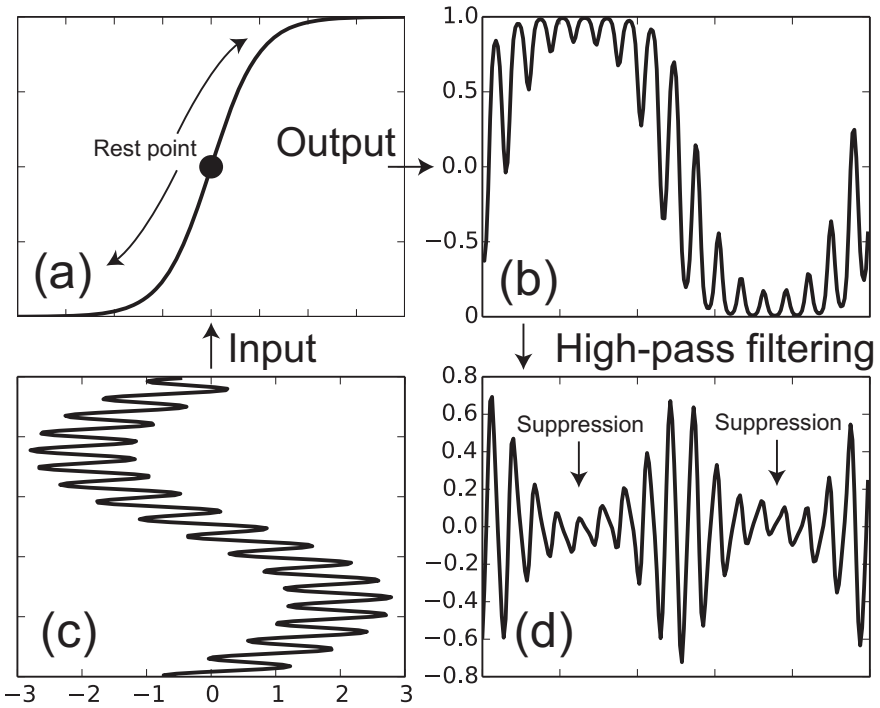

Figure 5.1: Schematics of the point operation concept for 2TS proposed by Geisler and Nuttall [57]; (a) a saturating IO curve, (c) two-tone input and (b) output. (d) The output with its low frequency components removed.

5.2.2 Vector subtraction theory

We propose vector subtraction as an alternative means of handling suppression. Conventionally, suppression is calculated by subtracting the mutual suppressive output (response to simultaneous sinusoidal inputs) from the self-suppressive output (response to sinusoids with no temporal overlap). Self-suppression and two-tone suppression are formulated as separate vectors. We also define the vector space set, in which the probe and suppressor input frequencies are represented as independent axes (Fig. 2). The self-suppression vector is calculated by summing the saturation function responses to the pure tones; the two-tone suppression vector expresses the pair of tones input to the saturation function. Vector subtraction then gives the difference between the self-suppression and two-tone suppression.

We now mathematically formulate self-suppression, two-tone suppression and their difference. First we express the nonlinear saturation function G(ξ) as a

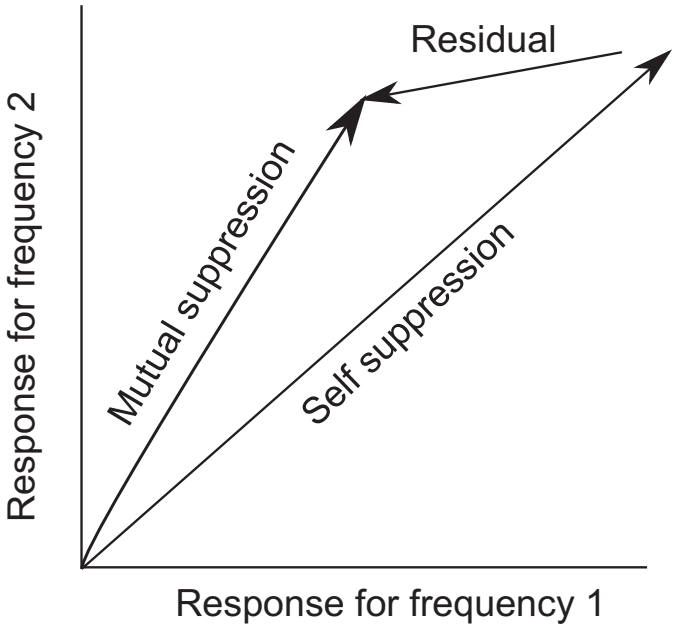

Figure 5.2: Vector representation of 2TS in the self-suppressed and two-tone suppressed states. Self-suppression and two-tone suppression result from two temporally separated sinusoids and simultaneous input of two sinusoids, respectively. The residual is a vector representing the difference between the two states.

third-order Taylor expansion:

$$\mathrm{G}\left(\xi\right) = \tanh\left(\xi\right) \simeq \xi - \frac{\xi^3}{3}. \tag{5.1}$$

Denoting the two sinusoidal inputs as $\xi_1 = A_1 \sin\theta_1$ and $\xi_2 = A_2 \sin\theta_2$, their outputs are calculated as

$$\begin{aligned} \mathrm{G}\left(\xi_1\right) &\simeq \left(A_1 - \frac{A_1^3}{4}\right)\sin\theta_1 + distortions \\ \mathrm{G}\left(\xi_2\right) &\simeq \left(A_2 - \frac{A_2^3}{4}\right)\sin\theta_2 + distortions. \end{aligned} \tag{5.2}$$

In their respective one-dimensional spaces θ_1 and space θ_2, these outputs equal ξ_1 and ξ_2, when A_1 and A_2 are substantially less than 1, and saturate when A_1 and A_2 are approximately greater than 1. When two sinusoids are simultaneously input as a two-tone suppression, the output is

$$\mathrm{G}\left(\xi_1+\xi_2\right) \simeq \left(A_1 - \frac{A_1^3}{4} - \frac{A_1A_2^2}{2}\right)\sin\theta_1 + \left(A_2 - \frac{A_2^3}{4} - \frac{A_1^2A_2}{2}\right)\sin\theta_2 + distortions. \tag{5.3}$$

The nonlinear output calculated by Eq. (5.3) clearly differs from that of self-suppression (such as the superposition of Eq. (5.2)). In Eq (5.3), the saturations

generated by the pair of sinusoids interfere with each other. The output can now be represented in a two-dimensional θ_1–θ_2 space. To preserve the unique property of Eq. (5.3), the difference between the two-tone and self-suppression is expressed as

$$\mathrm{G}\left(\xi_1+\xi_2\right)-\left(\mathrm{G}\left(\xi_1\right)+\mathrm{G}\left(\xi_2\right)\right)\simeq\begin{cases}-\frac{A_1^2A_2}{2}\sin\theta_2 & \text{if } A_1\gg A_2\\ -\frac{A_1A_2^2}{2}\sin\theta_1 & \text{if } A_1\ll A_2.\end{cases} \tag{5.4}$$

Equation (5.4) indicates that the difference between the two outputs is reduced by the higher-amplitude sinusoid.

5.2.3 Two-tone suppression in outer hair cell model

The OHC model has been proposed in Section 3.3 and has the nonlinearity based on the machanoelectric transducer $\mathrm{G_{tr}}$. Figure 5.3 show the vector differences of the mechanoelectric transducer $\mathrm{G_{tr}}$ (modified by Eq. (3.20)) and the simple feedback system including the the mechanoelectric transducer $\mathrm{G_{tr}}$ for two arbitrary frequencies f_1 and f_2 under the conditions of self-suppression $\mathrm{G_{tr}}(\xi_c(f_1)+\mathrm{G_{tr}}(\xi_c(f_2)$ and two-tone suppression $\mathrm{G_{tr}}(\xi_c(f_1)+\xi_c(f_2))$. The vectors point vertically or horizontally when $|\xi_c(f_1)|\gg|\xi_c(f_2)|$ and $|\xi_c(f_1)|\ll|\xi_c(f_2)|$. This phenomenon reflects the output reduction by the stronger input, which can be calculated by the saturation function Eq. (5.4).

5.3 Simulation method

Model is mechanical representation.

The frequency f_p of the probe tone was 6000 Hz and the frequencies f_s of the suppressor tone were varied from 1000–9000 Hz in 100-Hz steps (excluding 6000 Hz). The intensities L_p and L_s were increased from 20 to 80 dB in 10-dB steps. The probe frequency f_p is usually set to the characteristic frequency (CF) of the cochlear region ($x = 7.9$ mm), defined as the frequency of maximum excitation at 0 dB input. Each of the two primary tones was simultaneously presented for 55 ms, with rise/fall times of 5 ms. The model outputs were recorded for 10 ms, starting 40 ms after tone presentation to allow the system to reach steady state. In the time domain, the model outputs were the BM velocity $\dot{\xi}_b\left(x,t\right)$ and the BM displacement $\dot{\xi}_b\left(x,t\right)$, which were separated into probe tone and suppressor tone components. In the frequency domain, the outputs were the BM velocities $\dot{\xi}_b\left(x,f_p\right)$ and $\dot{\xi}_b\left(x,f_s\right)$, and the BM displacements $\xi_b\left(x,f_p\right)$ and $\xi_b\left(x,f_s\right)$. These

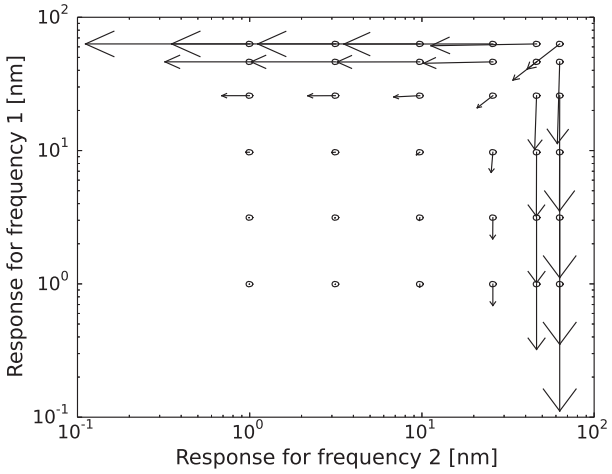

(a) $\xi_c^{nl} = \mathrm{G_{tr}}(\xi_c)$

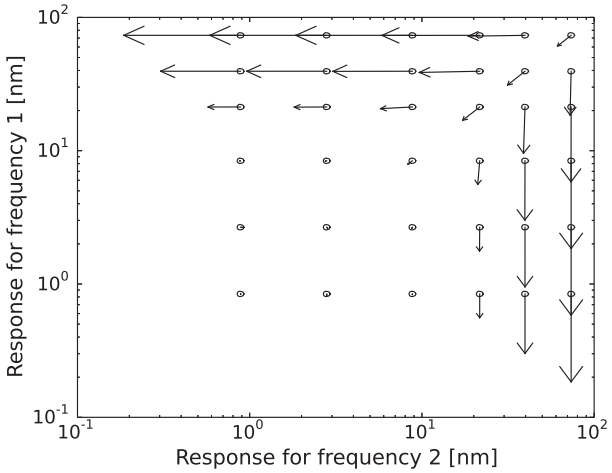

(b) $\xi_c^{nl} = \mathrm{G_{tr}}(\xi_c^{nl}) + \xi_c$

Figure 5.3: Residual vectors in the hair cell process for inputs of two arbitrary frequencies with amplitudes ranging from 1 nm to 100 nm.

components were obtained by fast Fourier transform (FFT) of their counterparts in the time domain.

5.4 Result

5.4.1 Input dependence

he frequency dependence of two-tone suppression at L_p = 20, 40, 60, and 80 dB is shown in Fig. 5.4(a)–(d). Clearly, the amount of suppression reduces as L_p increases.

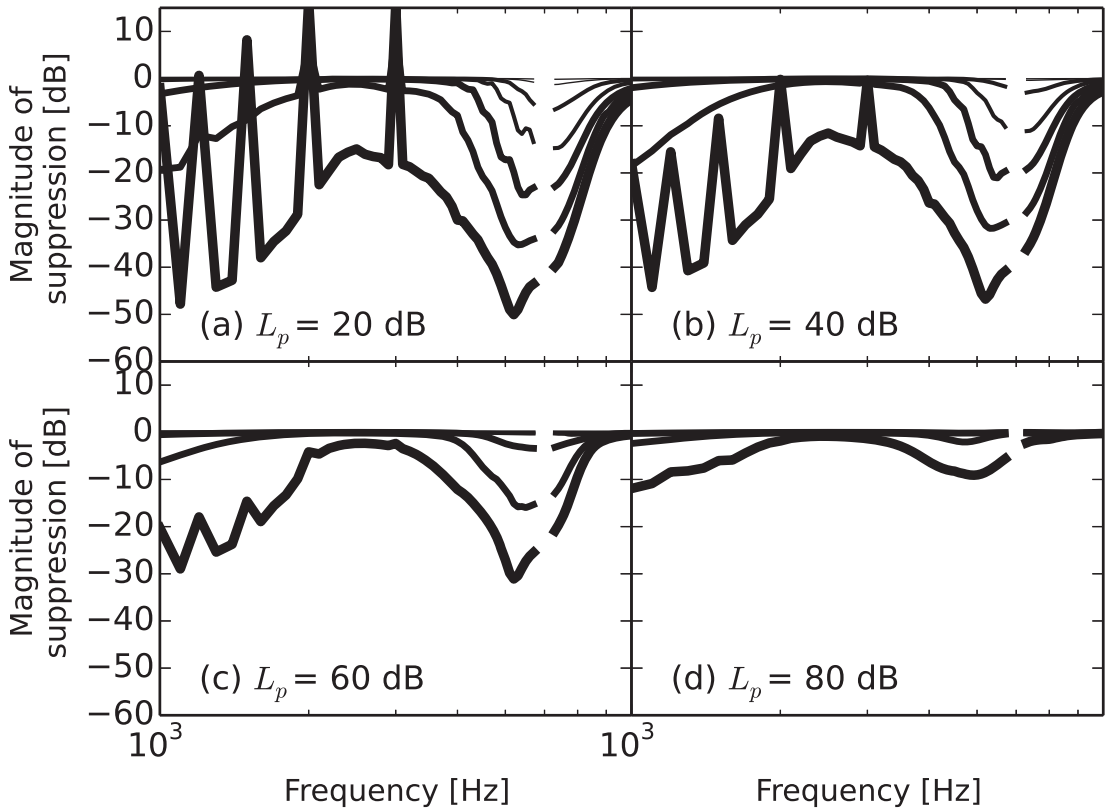

Figure 5.4: Suppression (ordinate) of a 6-kHz probe tone at (a) $L_p = 20$ dB, (b) $L_p = 40$ dB, (c) $L_p = 60$ dB, and (d) $L_p = 80$ dB by a suppressor tone as a function of suppressor frequency (abscissa). The intensity L_s is varied from 80 dB (thickest line) to 20 dB (thinnest line) in 10 dB steps. In the absence of a suppressor tone, the curves are normalized by the probe displacement.

First let us examine Fig. 5.4(a), in which the probe level L_p is 20 dB. At a suppressor level of 80 dB (darkest line) and suppressor frequencies of 4000 and 6500 Hz, the suppression is at least –40 dB. An interesting effect is the sharply reduced suppression at suppressor frequencies of 1000, 1200, 1500, 2000 and 3000 Hz (= CF/6, CF/5, CF/4, CF/3 and CF/2, respectively). In fact, at these frequencies the suppression crosses the 0 dB line, indicating amplification of the BM motion by the probe. At suppressor frequencies just below the CF, the suppression steadily increased with suppressor level. However, when $f_s \ll CF$, the suppression increased drastically with suppressor level (exceeding 60 dB). Notches were not observed, and suppression was strong ($\sim$ –40 dB) at low suppressor frequencies.

At $L_p = 40$ dB (Fig. 5.4(b)), the suppression pattern matches that at $L_p = 20$ dB, but the suppression peaks and notches are less prominent. At $L_p = 60$ dB (Fig. 5.4(c)), suppression is reduced at all suppressor frequencies, reaching a

maximum of –30 dB at 4000 Hz. Notches and peaks disappear. At L_p = 80 dB (Fig. 5.4(d)), little suppression occurs and the maximum is –10 dB at around f_s = CF.

Figure 5.5 plots the BM iso-displacement contours at the CF produced by two-tone excitation, as functions of probe and suppressor level. The numbers at the right are the frequency ratios. The left and right columns show the BM displacements by the probe and suppressor, respectively. Both probe and suppressor levels increase from 20 dB (thin lines) to 80 dB (thick lines) at the four investigated frequency ratios (f_s/f_p = 0.18, 0.95, 1.05, and 1.50 (top to bottom)). At f_s/f_p = 0.18, the BM displacement is constant at suppressor levels below 50 dB. However, at suppressor levels of 50 dB and above, the BM displacement by the probe decreases with increasing suppressor level. The same trend is observed at f_s/f_p = 0.95 and 1.05. At f_s/f_p=1.50, the suppressor only slightly affects the BM displacement. In the suppressor plots, the BM displacement is independent of probe level at f_s/f_p = 0.18. At f_s/f_p = 0.95 and 1.05, the BM displacement by the probe decreases with increasing probe level. At f_p/f_s=1.50, it displaces by under 1 nm.

5.4.2 Rate of suppression

The rate of suppression (ROS) measure is computed as the slope of the displacement IO function. A large ROS value indicates a rapid suppression response; conversely, zero ROS indicates no suppression. ROS is a function of the frequency ratio and the relative levels of the primaries. As shown in Fig. 5.6, suppression gently increases. The ROSs plotted in Fig. 5.6 are calculated from the I/O functions shown in Fig. 5.5. At f_s/f_p = 0.18, the ROS curves are maximized (at approximately 2.0 dB/dB) at the highest suppressor level and the lowest probe level. The ROS maximum was found to decrease with increasing probe level. The ROS is 0 dB/dB at low suppressor levels, and increases as the suppressor level increases from 60 dB. At f_s/f_p = 0.95 and 1.05, the ROS is maximized at 1.0 dB/dB. The curves plateau at mid-range suppressor levels and systematically shift toward higher levels with increasing suppressor level. The maximum ROS is below 0.1 dB/dB at f_p/f_s = 1.50, and unresponsive to suppressor level.

The previous results were obtained under four suppressor frequency conditions. To investigate how the ROS behaves over a wider range of suppressor frequencies (600–9000 Hz), we plotted the maximum ROS as a function of suppressor fre-

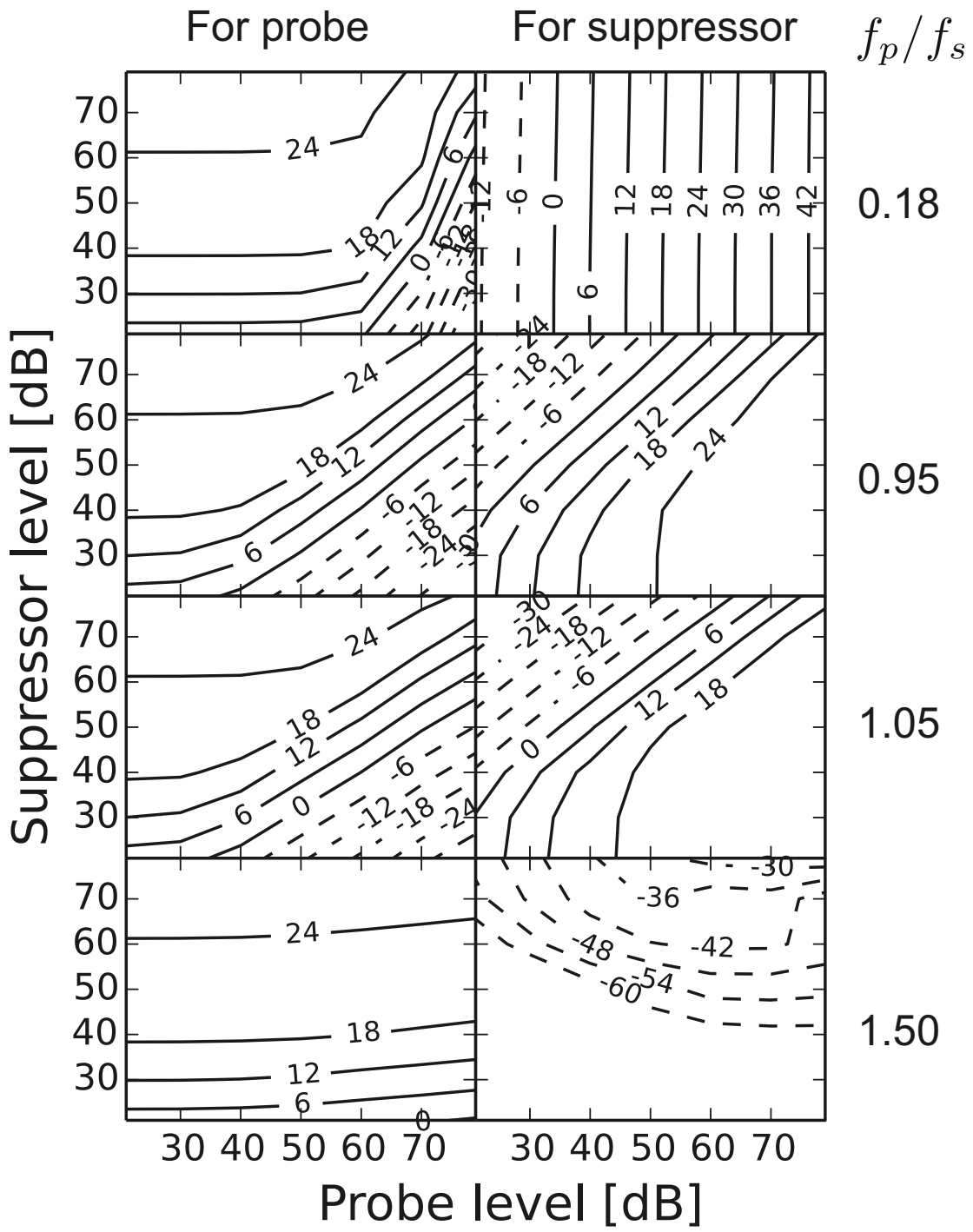

Figure 5.5: BM iso-displacement curves for excitation by probe (left panels) and suppressor (right panels) as functions of suppressor level L_s and probe level L_p. The probe tone was set to the CF (6000 Hz) and the suppressor tones were 4200 Hz, 5700 Hz, 6300 Hz, and 8000 Hz (rows top to bottom). The indexes on the curve are the displacements (relative to the reference displacement of 1 nm). Contours are plotted in 6 dB steps. Dashed lines indicate displacements below 1 nm.

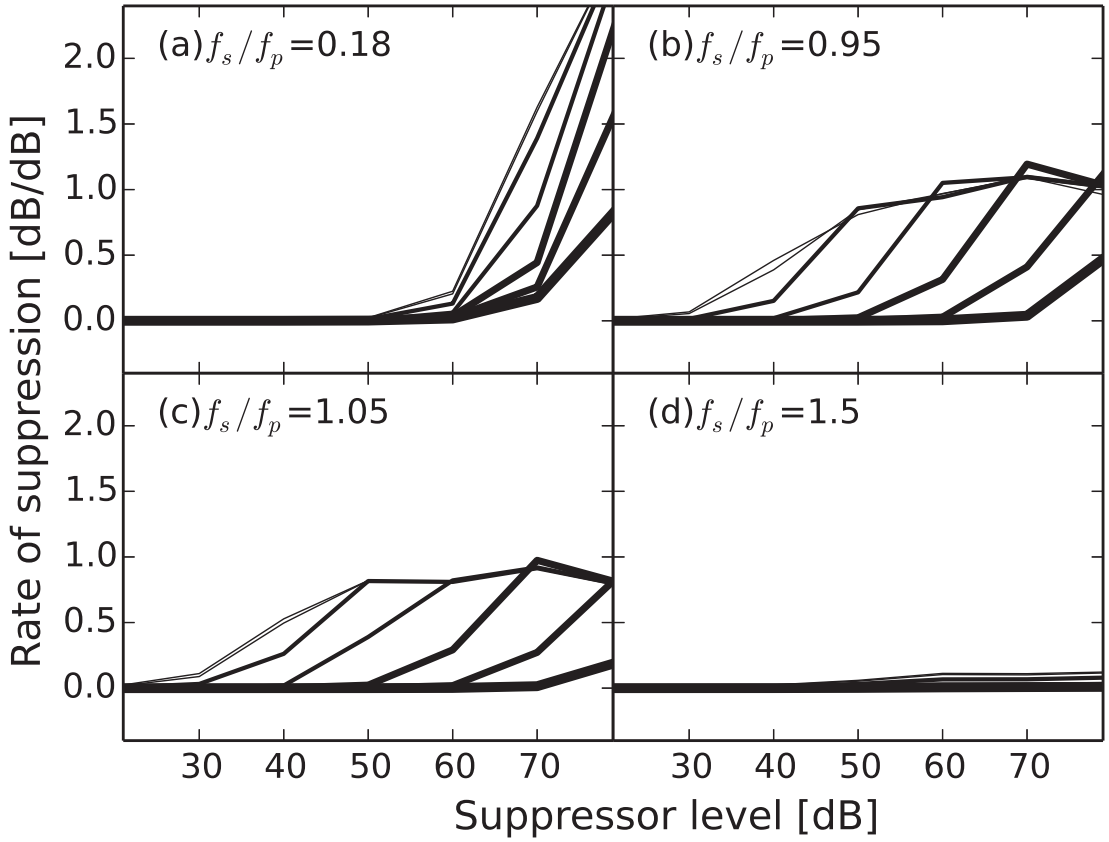

Figure 5.6: Rate of suppression (ROS) of the probe tone computed as the slope of the displacement I/O functions in Fig. 8 for four suppressor frequencies (specified as ratios f_p/f_s). Increasing line thickness indicates the increasing level of L_p (from 20 to 80 dB).

quency. The results are presented in Fig. 5.7. At $f_s \ll CF$, peaks and notches appear in the maximum ROS curves. The average ROS is approximately 2.1 dB/dB, with the exception of two suppressor frequencies (CF/2, CF/3, CF/4, CF/5 and CF/6) at which virtually no suppression is observed (see Fig. 5.4). At $f_s \geq CF$, the maximum ROS values decrease with increasing suppressor frequency.

To summarize the effects of CF and suppressor frequency on the ROS, the maximum ROS was fitted by the three-parameter model proposed by [60]. This model expresses the maximum ROS, α, as a function of the CF and suppressor frequency f_s:

$$\alpha = a + b \cdot g(f_s/CF), \tag{5.5}$$

$$g(f_s/CF) = \begin{cases} \log_{10}(f_s/CF/c) \text{ if } f_s/CF > c \\ 0 \text{ otherwise} \end{cases}, \tag{5.6}$$

where a denotes the plateau maximum at low suppressor frequencies, b is the slope

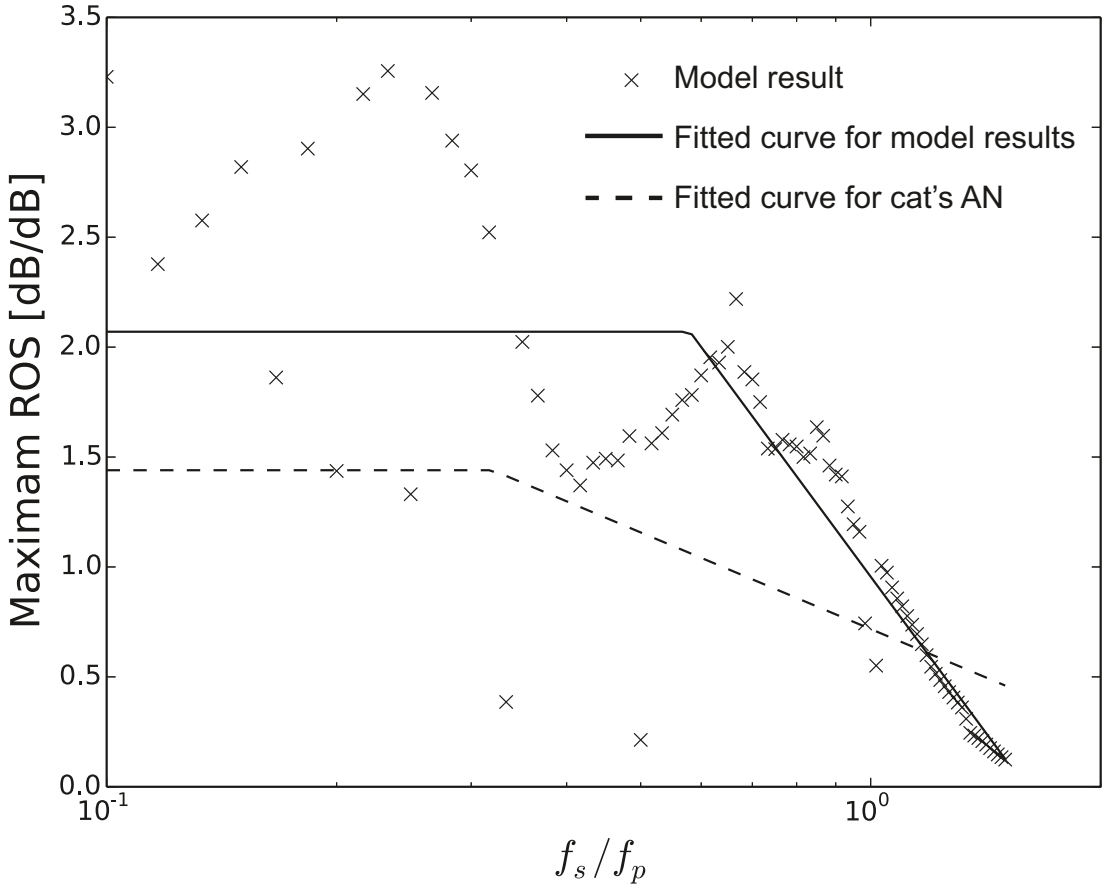

Figure 5.7: Scatter plot of maximum ROS values. Individual data points are plotted from the simulated ROS functions with the probe at CF. The solid line plots the model predictions according to Eq. (7). The parameter values of a, b, and c, obtained from the simulation results, are 2.06, 5.35, and 0.62, respectively. The dashed line plots the model predictions of Eq. (7) with a, b, and c set to 1.44, 1.46, and 0.32, respectively. These values were obtained from auditory nerve data ([60]).

around f_s/CF =1, and c is the location of the breakpoint in Eq. 5.5. The solid line in Fig. 5.7 is obtained by fitting the maximum ROS to Eq. 5.5. This model captures the main trends of the maximum ROS. The parameter values in this study were higher than those extracted from auditory nerve data ([60]), which are plotted as the dashed line in Fig. 5.7.

5.4.3 Temporal feature

Figure 5.8 shows the CF response waveforms at two suppressor frequencies (1100 Hz and 4000 Hz). The input levels of the probe and suppressor are fixed at 50 dB and 70 dB, respectively. Frequency components lower than CF were removed by

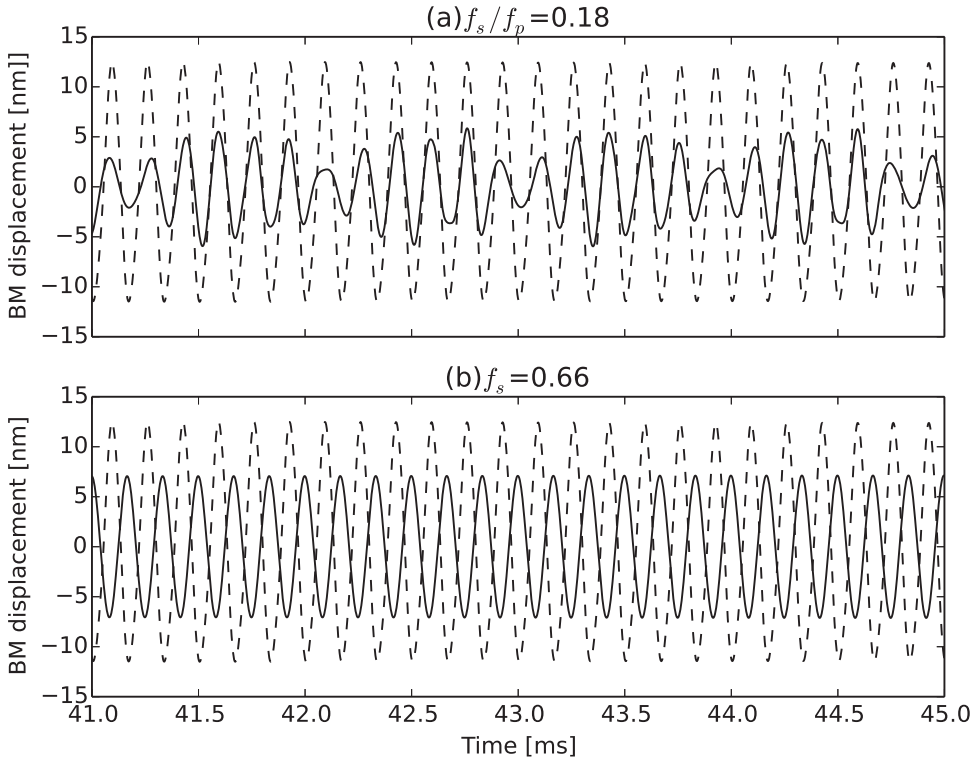

Figure 5.8: Temporal BM response at CF equaled to 6000 Hz. (Dashed) CF-alone responses at $L_p = 40$ dB. (Solid) CF responses obtained with two suppressors at $L_p = 40$ dB and $L_s = 80$ dB. (Top) $f_s = 1100$Hz (Bottom) $f_s = 4000$ Hz. The responses are filtered to remove the suppressor effects.

low pass filtering at $f_s/f_p = 0.18$. Second and third harmonics at $f_s/f_p = 0.66$ were removed by an additional band-pass filter. Response amplitudes must have been reduced by the suppressor, because the CF-alone response is approximately 10 nm (see the dashed line). At $f_s/f_p = 0.18$, the envelope of the waveform is modulated at the suppressor frequency. At $f_s/f_p = 0.66$, this low-frequency modulation disappears.

5.4.4 Cochlear impedance

Impedance $Z_{cp}(\omega)$ in the micromechanical cochlea model has been defined as [30]

$$Z_{cp}(x,\omega) = Z_1(x,\omega) + \frac{Z_2(x,\omega)\left(Z_3(x,\omega) + \gamma(x,\omega)Z_4(x,\omega)\right)}{Z_2(x,\omega) + Z_3(x,\omega)} \tag{5.7}$$

$$\gamma(x,\omega) = \frac{\xi_c^{nl}(x,\omega)}{\xi_c(x,\omega)}, \tag{5.8}$$

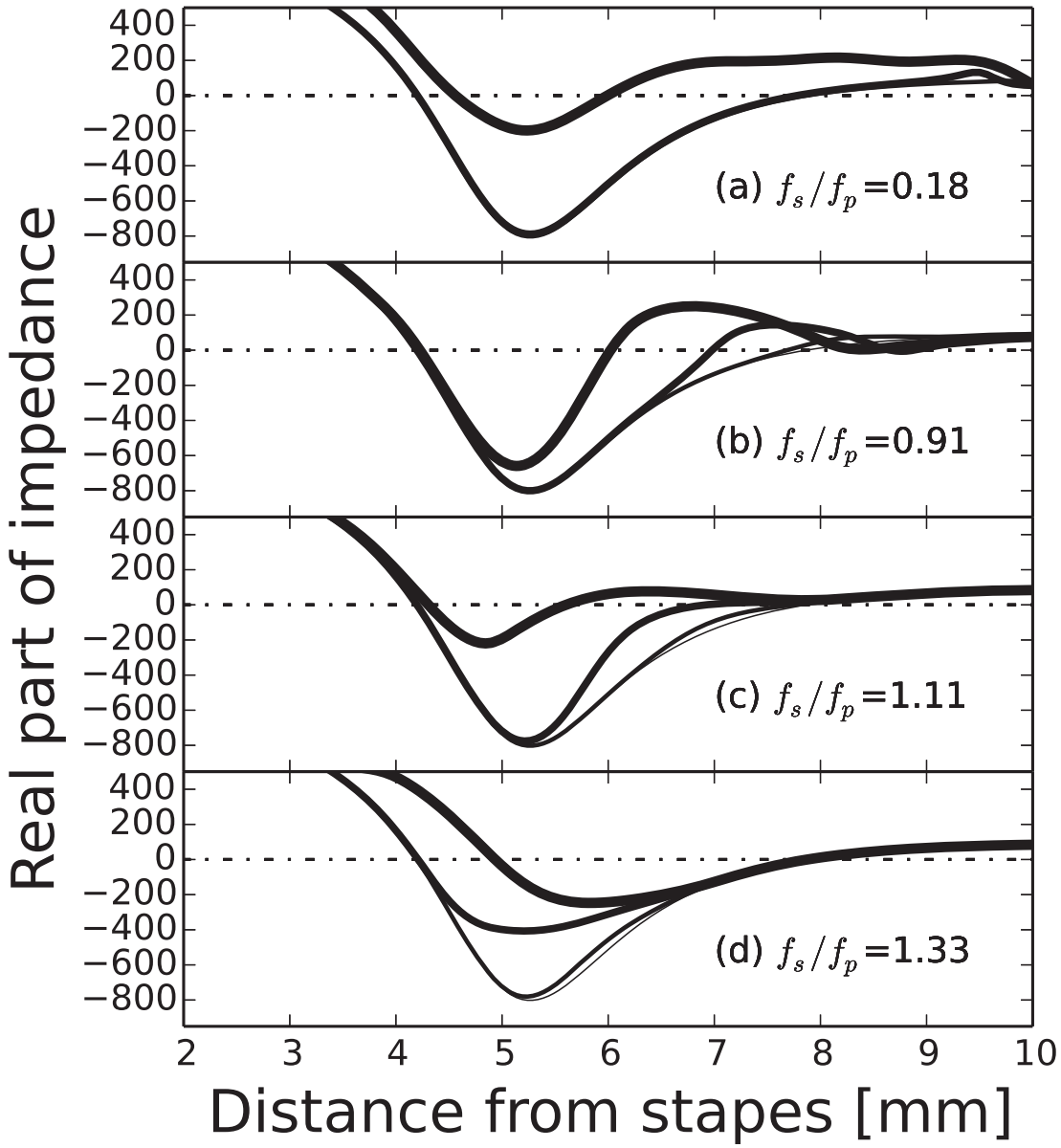

Figure 5.9: Real part of the impedance $Z_{cp}(x, \omega)$ along the cochlear length for four ratios (a)–(d) of f_p/f_s and angular frequency ω (calculated as $2\pi f_p$ rad/s). The x-axis ranges from 2 to 10 mm and the traveling wave of the probe is maximized at 8 mm. The probe level is 20 dB, and the suppressor level is increased from 20 dB (thin lines) to 80 dB (thick lines) in 20-dB steps.

where Z_1, Z_2, Z_3, and Z_4 are the respective mechanical impedances of the BM, TM, HB, and OHC in Fig. 3.1 and ω is the angular frequency. However, Eq. 5.7 is expressed in terms of frequency whereas the model is solved in the time domain. Therefore, the velocities in the time domain were converted to the frequency domain by FFT.

Figure 5.9 plots the impedance Z_{cp} under the four conditions in Fig. 5.4

with $L_p = 20$ dB. The traveling wave peaks at approximately 8.0 mm from the stapes. Cochlear amplification is induced by negative values of the real part of the impedance, which are generated by the active OHC model. At $f_s/f_p = 0.18$, both real parts follow the same trend at $L_s = 20$, 40 and 60 dB. At $L_s = 80$ dB, the real part of the impedance becomes positive around a cochlear length of 7.5 mm. At $f_s/f_p = 0.95$ and 1.05, the real part of the impedance becomes increasingly more positive, and the suppressor level covers a wider range of cochlear lengths than when $f_s/f_p = 0.18$. At $f_p/f_s = 1.33$, the real part of the impedance becomes less negative around a cochlear length of 5.0 mm as the suppressor levels increase, but is independent of input level around 8 mm, the location of the traveling wave peak.

5.4.5 Overall response

To examine the overall response of the cochlear model, the energy of BM vibration E_b was evaluated. The relevant energy of the BM vibration can be experimentally quantified by measuring the power in the cochlear fluid surrounding the BM [61]. Also relevant is the longitudinal coupling of the BM to the tectorial membrane [62]. Under our simulation conditions, the BM vibrations of both probe and suppressor can be considered as simple harmonic motions; this assumption is validated by FFT-ing the steady-state output of the model. According to Meriam and Kraige ([63]), the energy $E_b(\omega)$ of the BM vibration is given by

$$E_b(\omega) = \frac{1}{2} K(\omega) b^2 \Delta x^2 \sum_{n=0}^{N-1} |\xi_n^b(\omega)|^2, \tag{5.9}$$

where $K(\omega) = m_1\omega^2$ ($\omega = 2\pi f$), m_1 is the BM mass per unit area, b is the width of the BM, and Δx is the segment length. The calculation results are plotted in Fig. 13.

At $f_p/f_s = 0.18$ (top left of Fig. 5.10), the energy of the probe is clearly suppressed by the higher energy of the suppressor, whereas the energy of the suppressor is minimally reduced (note the slight shift toward the left). In the following cases ($f_p/f_s = 0.95$ and 1.05), the energy is greatly suppressed by the companion tone. Finally, at $f_p/f_s = 1.33$, the energy of the probe is suppressed by the suppressor except at very high probe energies, when the energy of the suppressor is weakened (as evidenced by the left-pointing arrows).

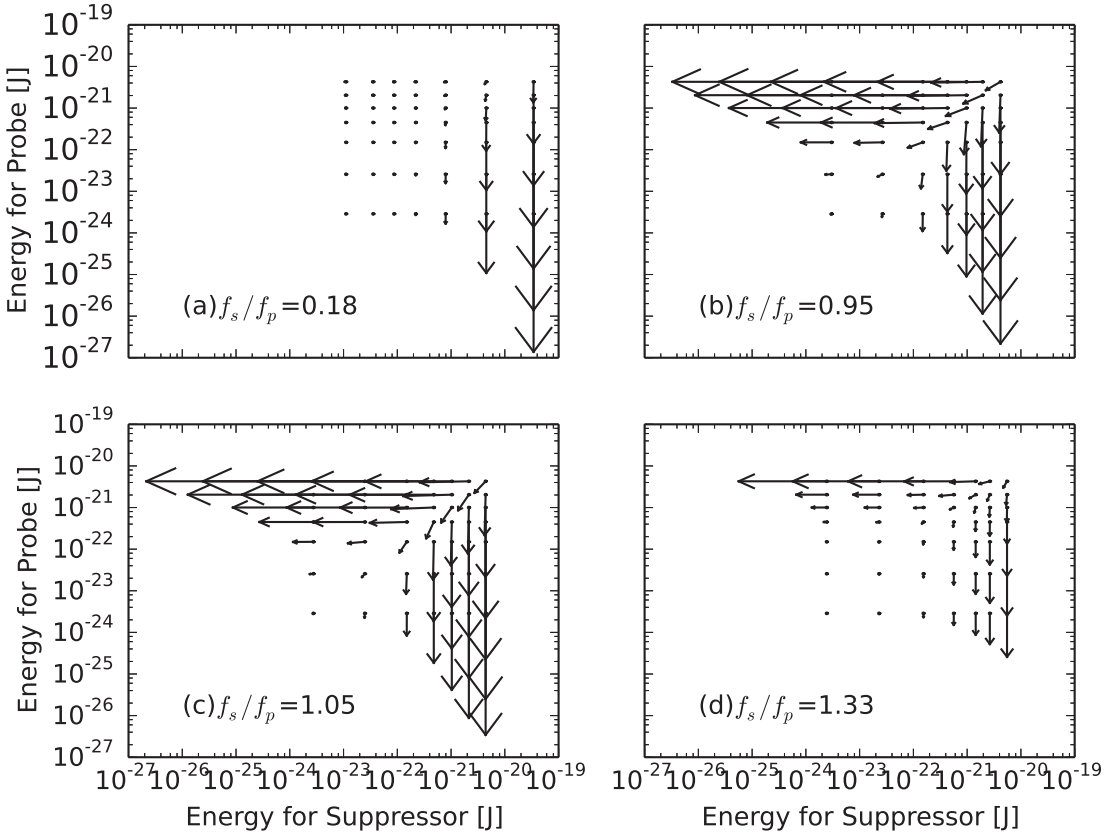

Figure 5.10: Vibration pattern of probe and suppressor expressed in terms of BM energy. Circles indicate BM vibration energy under the no-suppression condition (i.e., no temporal overlap between the probe and the suppressor). Arrows indicate shifts in BM vibration energy from the condition of no temporal overlap to the simultaneous input of probe and suppressor.

5.5 Discussion

5.5.1 Mechanisms of two-tone suppression

This paper has sought to reproduce the experimental findings of 2TS within a nonlinear cochlear model. In this section, we discuss the likely mechanisms underlying the simulation results. Basically, our model supports two mechanisms of 2TS generation: the point operation theory and the vector subtraction theory (developed in Sec. 5.2.1 and 5.2.2, respectively). Regarding the point operation theory, the phasic suppression shown in Fig. 5.1 is similar to the 2TS obtained from the experimentally determined BM responses shown in Fig. 5.8(a). Furthermore, the suppressor reduced the probe responses only at $f_p/f_s = 0.18$ (see Fig. 5.10(a)). Tonic suppression, or response suppression of the weaker tones by the stronger

tones, was enabled at higher suppressor frequencies (see Fig. 5.10(b)–(d)). This phenomenon results from the vector subtraction theory, assuming that the OHCs are the sole nonlinear elements. Under these conditions, the theoretical residual vectors are similar to the 2TS obtained from the experimental BM responses shown in Fig. 5.10(b)–(d).

As shown in Fig. 5.10, the BM vibration energy of both suppressor and probe ranged from 20^{-25} to 20^{-20} J. Comparable values around the peak of the traveling wave have been reported in experimental studies ([61]). The suppression is maximized at 50 dB (Fig. 5.4), and stronger tones suppress the response to weaker tones (Fig. 5.10(b)–(d)). The level-dependent point responses in Fig. 5.5 show that both probe and suppressor are suppressed by the higher-level companion when their frequencies are close, but this trend disappears when the frequencies are very different. Suppression occurs around the peak of the traveling wave, indicating problems with employing point responses.

2TS originates from two tones of different frequencies. The simulated level- and frequency-dependencies of 2TS Figs. 5.4 and 5.5 match the experimental results of Rhode [59]. Therefore, 2TS generation can be understood from the two-dimensional spreading behavior of compression in the OHC model (see Fig. 5.2). For this purpose, expressing both dimensions in frequency units is advantageous. In Fig. 5.5, the responses of the weaker probe or suppressor are suppressed by the stronger companion when the probe and suppressor frequencies are close. When the two frequencies diverge, the peaks of the traveling wave become widely spaced and each peak stimulates separate populations of OHCs. In Fig. 4.2, the traveling wave peaks are well-separated, and the OHCs can amplify BM motion around the CF; conversely, the OCHs are unresponsive to low-side suppressor frequencies. Similar behavior has been reported in physiological studies [57]. However, at high suppressor frequencies, the suppressor affects the tail of the traveling wave of the probe, generating less and gentler suppression (Fig. 5.5).

Figure 5.7 reveals several features of the maximum ROS: (1) slow variation at low side frequencies, (2) a breakpoint below the CF, and (3) a minimum around the CF. According to Fig. 4.2, the BM response to a tone linearly increases with frequency at low side frequencies, but shows compressive growth around the CF. This suggests that the growth rates of the BM responses to a suppressor and a tone are identical. Similarly, the OCH inputs might behave linearly at low-side frequencies and compressively around the CF. The compressive growth of the OHC

output in response to a probe reduces the gain of the cochlear amplifier, leading to 2TS and compression.

Suppression is subdued and more gradual at the highest suppressor frequencies (Fig. 5.9(d)), which has implications for the traveling wave theory. From the peak of the traveling wave ($x \neq 8.0$ mm), the real parts of the impedance progressively shift toward zero around $x = 7.0$ mm, implying less cochlear amplification. According to deBoer and Nuttall [64], the amplification is lowered by negative-to-positive conversion of the real parts of the impedance, itself imposed by the neighboring peaks of the traveling waves. If true, this theoretical notion explains the reduced suppression under such conditions.

Panels (a)–(c) of Fig. 5.9, in which the probe is suppressed despite the changes in the real parts of the impedances at lower suppressor frequencies, are problematic. The real part changes from negative to positive around the peak of the traveling wave, as reported in deBoer and Nuttall [64]. The actual situation is unclear, but these findings collectively indicate that the OHCs around the peak of the traveling wave play the major role in 2TS, and that OHCs far from the peak are responsible for the lesser, more gradual, suppression at higher suppressor frequencies.

5.5.2 Comparison with previous works

The suppression reduced from 50 to 10 dB as the probe levels rose from 20 to 80 dB (see Fig. 5.4). In a previous experimental report, the suppression magnitude decreased from 35 to 5 dB as the probe level rose from 15 to 55 dB ([17]). Given that suppression depends on the state of the cochlea—it can reach 50 dB in an intact cochlea but is seriously impaired in a damaged one ([59])—these results are broadly comparable. In the current study, the ROS function plateaued at 1 dB/dB when the suppressor frequency approximated the probe frequency (see Fig. 5.6(b) and (c)). When the suppressor frequency was lower than the probe frequency (Fig. 9a), the onset of ROS growth was shifted upward, reaching as high as 2 dB/dB. Our simulated ROS values can also be compared with previous experimental data ([59]). The present results reveal breakpoints and slow variation in the maximum ROS values at low side suppressor frequencies (see Fig. 5.7). However, these results differ from the experimental findings of Rhode [59], in which the maximum ROS monotonically decreases with increasing suppressor frequency.

According to some previous AN experiments, the maximum ROG ranges from 1 to 3 dB/dB for below-CF suppressors, and rapidly decreases with increasing sup-

pressor frequency [60]. This finding is consistent with the model results plotted in Fig. 5.7. However, for below-CF suppressors, the distributions of the maximum ROG values differ between the results of AN and BM experiments. The filtering function of the IHC may account for such discrepancy [65], but this suggestion is unsupported by our model results. Instead, it appears that mechanical transduction of the BM directly affects neural information coding in the AN. Whether mechanical events fully account for neural data was discussed for below-CF suppression in the previous subsection.

The suppression at low side frequencies demonstrated phasic temporal behavior (see Fig. 5.8(a)). However, at frequencies approximating the CF, this trend was replaced by a tonic temporal feature (Fig. 5.8(b)). Phasic and tonic suppression has been experimentally observed at suppressor frequencies up to 4 kHz; at higher suppressor frequencies, the suppression is predominantly tonic. The CF in these experiments was around 17 kHz [57].

5.5.3 Transferring the vector subtraction theory to other models

The two-dimensional property of our model should be easily transferable to other models, including transmission line models, phenomenological models of the cochlea, and simple models of the cochlear partition. Regardless of fluid coupling, 2TS should emerge in the overall BM responses in present transmission line models (see Fig. 5.10). The two-dimensional property of the OHC model (expressed by Eqs. (5.3) and (5.4) and illustrated in Fig. 2C) derives from the feedforward system in Eqs. (5.1) and (3.22). However, as described in Sec. II.C, the cochlear feedback system exists within the OHC system. Despite these different starting points, the saturation function exhibits 2TS in the BM model, as shown in Fig. 5.10. Therefore, the two-dimensional property of the saturation function can probably simulate 2TS on the BM in other cochlear models.

Like the present model, existing transmission line models [32, 66, 34, 36] generate 2TS using a single active, nonlinear element. Therefore, we can compare the 2TS mechanisms of previous models with those examined here. Our parameter values are outside the experimentally determined parameter range because our model is somewhat simplified. More realistic parameter values were adopted in an elaborate transmission line model ([67]). Moreover, the motion of the organ of Corti is difficult to describe because this organ constitutes a variety of tissues,

whose stiffness varies in complex ways [68].

The two-dimensional property of the saturation function is applicable to phenomenological models, which similarly adopt an I/O function. A phenomenological model generally assumes a feedforward system [39, 40]; for this reason, it can be well-matched to a two-dimensional saturation function.

Simple models of the cochlear partition, such as the present model and nonlinear oscillator models, provide identical descriptions of activities that ignore fluid coupling. The nonlinear oscillator model replicates the essential nature of 2TS, namely, that a primary tone suppresses or is suppressed by another primary tone [69] (see Fig. 5.10). The active nonlinear processes in the nonlinear oscillator model have been related to hair bundle motility [10]. Alternatively, the active process might be explained by somatic motility [6]. The potential importance of mechanoelectric transduction and somatic motility in the active process has also emerged in the oscillator model [70]. These studies support the idea that the OHC mechanoelectric transfer function influences the active nonlinear process in cochlear mechanics.

5.6 Summary

To explain two-tone suppression induced by active and nonlinear process in the cochlea, we developed a special saturation function with a distinctive residual response to a two-tone input. This function was incorporated into the nonlinear transmission line model, which is similar to others reported in the literature. Our model displays two types of suppressive mechanisms, depending on the suppressor frequencies. 2TS was realized by the vector properties and the point operation in the saturation function for near-CF suppressors and low-side suppressors, respectively. Our basic formulations are readily adaptable to other cochlear models. Such a low degree-of-freedom model could also be useful for investigating other cochlear nonlinearities. Our work has demonstrated how a single cochlear variable—the BM vibration energy—can explain nonlinear cochlear dynamics.

Chapter 6

Distortion product

6.1 Introduction

Cochlear nonlinearities depend on sound pressure level with in the intact cochlea [52]. As one of cochlear nonlinearities, distortion products (DPs) is a response to an absent tone when a two-tone pair is transmitted to the hearing apparatus. This phenomenon was observed in the auditory nerve half a century ago [19], in the otoacoustic emission [20] and on the basilar membrane [21, 22]. Amplitudes of DPs depend on the sound pressure level in the animal measurements [71, 72]. These level dependence of DP can be explained explicitly by a saturation function that generates a modulation effect when a two-tone pair is presented [55].

Mechanoelectric transduction in the outer hair cells (OHC) produces a saturation function that has been supposed to be the source of nonlinearities in cochlear mechanics, and can be described by a second-order Boltzmann function [56]. The second-order Boltzmann function modeling the mechanoelectric transduction in the OHC also generated DPs depending on the input levels [46]. Furthermore, a simple phenomenological feedback model including the second-order Boltzmann function showed DPs [73]. However, it has not yet been reported the effect of DP that deference between feedfoward and feedback is.

One of the source of these nonlinearities is commonly believed to be a saturating process in the cochlea. The transmission line models of the cochlea well predicted DPs that is obtained from a dynamic interaction including a saturating feedback [37, 35, 36]. However, clear explications for DPs within the transmission line have not yet been reported because complex structure [37] and many parameters [35]. In order to interpret those results, simplified models are required.

As basic cochlear nonlinearity depending on sound pressure level, the compres-

sive growth in input–output (IO) function of the cochlea has been introduced. The experimental measurement showed that a slope value was less than 0.2 dB/dB for sound pressure levels above about 30 dB SPL [59]. This compressive nonlinearity has been also believed to be generated by the saturation function located in the OHC. However, a slope of the saturation function is completely compressed, 0 dB/dB, for higher input levels. To fit the compressive IO curve, simple phenomenological feedback models including a saturation function have been used [74, 75].

Frequency selectivity is a central part of cochlear function, and cochlear models accounting for frequency selectivity can be realized phenomenologically by filter banks [40, 39]. These phenomenological models can account for cochlear nonlinearities as shown in the transmission line model [37, 35, 36]. Despite good fittings for these cochlear nonlinearities, most of the phenomenological models are feedfoward models. Instead of a saturation function, they apply a power-law nonlinearity to generate compressive growth.

To account for the mechanisms that produce DP depending on input level in the cochlea, the aim of this paper is to introduce the significance of feedback on the saturation function. Two simple phenomenological models, a power-law nonlinear model and a transmission line model of the cochlea are proposed. These simple models form either feedfoward or feedback and consist of one saturation function and one gain factor. The power-law nonlinear model shows compressive growth without saturation function. A transmission line model of the cochlea including a saturating feedback are developed. The models are tested for both single and dual tones.

6.2 Model

6.2.1 Modulation in saturation function

Modulation in the saturation function can account for DP [55]. In this section, we introduce modulation in the saturation function.

The equation of a saturation function that emits output y for input x is

$$y(t) = \mathrm{G}\left(x(t)\right), \tag{6.1}$$

where t is a time series and $\mathrm{G}\left(\cdot\right)$ is a saturation function. To analyze the saturation

function, we define it as

$$\mathrm{G}(x) = \tanh(x) \simeq x - \frac{x^3}{3}. \tag{6.2}$$

From third-order Taylor expansion, the saturation function can be explained by the above power series. Let $x(t)$ denote sum of two sinusoids $a_1 \sin(2\pi f_1 t) + a_2 \sin(2\pi f_2 t)$ where a_1 and a_2 represent an amplitude and f_1 and f_2 represent frequency. In this case, $y(t)$ includes harmonics $\{3f_1, 3f_2\}$ and DP $\{\ 2f_1 - f_2,\ 2f_2 - f_1,\ 2f_1 + f_2,\ 2f_2 + f_1\ \}$ that can be derived from the trigonometric addition formulas. Amplitudes of both harmonics and DP depend on the amplitude of input $x(t)$. For example, DP for $2f_1 - f_2$ is proportional to $a_1^2 a_2$.

6.2.2 Simple models

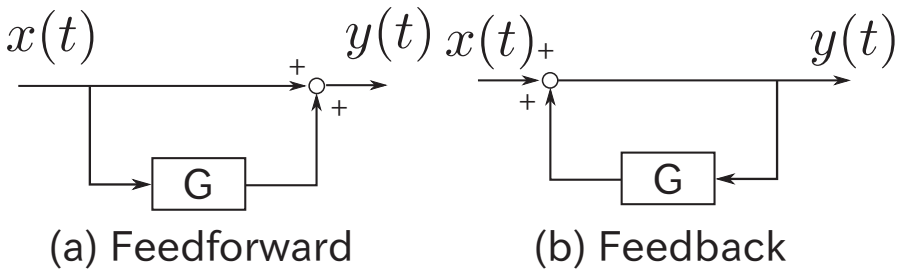

Figure 6.1: Block diagram of simple models. (a) Feedforward model. (b) Feedback model.

The feedback from the OHCs affects cochlear processing and is the amplification and the saturating process . An linear feedback model amplifying input $x(t)$ is

$$y(t) = ay(t) + x(t), \tag{6.3}$$

where a is gain factor ($0 \leq a < 1$). To transform above equation, an linear feedforward model is obtained:

$$y(t) = \frac{1}{1-a} x(t). \tag{6.4}$$

A simple feedforward model is proposed in Fig. 6.1(a). The equation of the feedforward model based on Eq. 6.4 including the saturation function G in Eq. 6.1 is

$$y(t) = \frac{1}{1-a} \mathrm{G}(x(t)) + x(t), \tag{6.5}$$

Table 6.1: Slope values for input-output property of the transmission line model over the input range 30 - 80 dB

Frequency [Hz]	1000	2000	4000	8000
Slope [dB/dB]	0.18	0.13	0.12	0.20

A simple feedback model is proposed in Fig. 6.1(b). To expand the linear model in Eq. 6.3, the equation of the feedback model including the saturation function G in Eq. 6.1 is

$$y(t) = a\mathrm{G}\left(y(t)\right) + x(t). \tag{6.6}$$

The gain factor a is set to 0.99. It was determined so that the outputs of the simple models at the lower input levels were higher by 40 dB relative to those of the model with no gain because the OHCs amplify BM motion over 40 dB [52].

6.2.3 Power-law nonlinear model

Compressive growth in the cochlear IO property can be fitted by a power-law nonlinearity [39]:

$$y = |x|^p \operatorname{sgn}(x), \tag{6.7}$$

where the power p is less than unity. The signum function is defined by

$$\operatorname{sgn}(x) = \begin{cases} -1 & for \quad x < 0 \\ 1 & for \quad x > 0 \\ 0 & for \quad x = 0 \end{cases}. \tag{6.8}$$

6.3 Simulation method

Each of the two primary tones was simultaneously presented for 65 ms, with rise/fall times of 5 ms. Recording of the model outputs started 40 ms after presentation of the tones (because the system requires sufficient time to reach steady state) and lasted 20 ms. In the time domain, the outputs of the model were BM velocity $\dot{\xi}_n^b(t)$ and BM displacement $\xi_n^b(t)$, which were separated into primaries $\xi_n^b(f_1)$ and $\xi_n^b(f_2)$ and distorted components (*e.g.* $\xi_n^b(2f_1 - f_2)$) in the frequency domain using the fast Fourier transform.

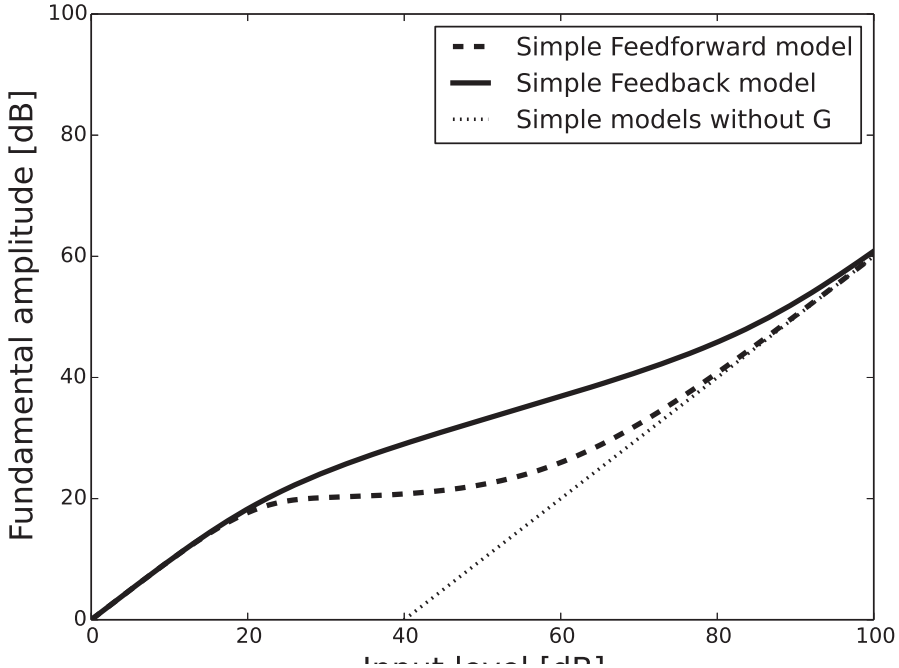

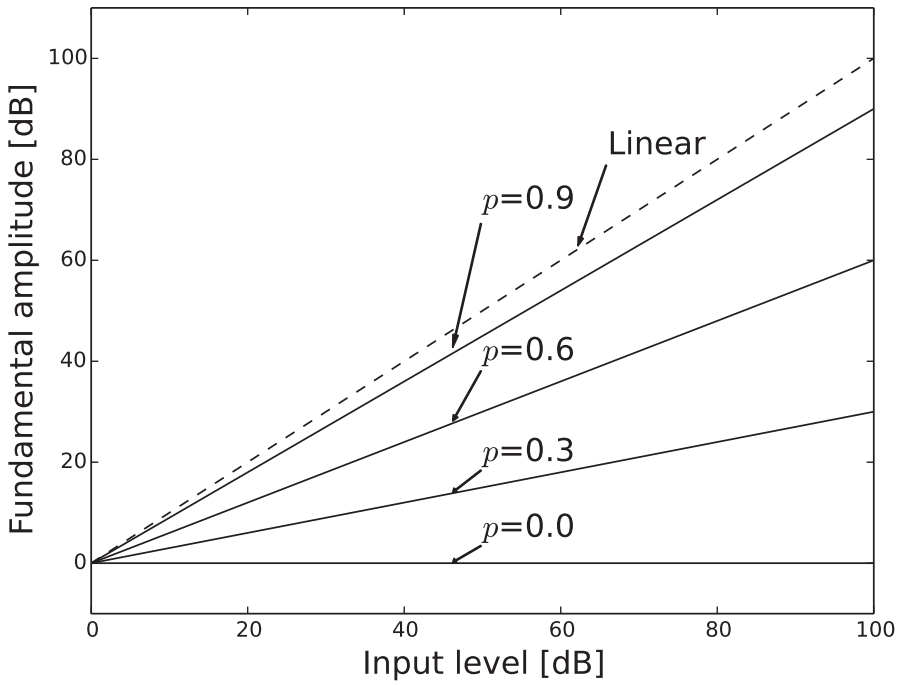

(b) Power-law nonlinear model

Figure 6.2: Input-output properties. Reference values are $y = 10^1$, $y = 10^{-1}$, $y = 1$ and $\xi_n^b = 1$ nm for the simple feedforward model, the simple feedback model, the power-law nonlinear model and the transmission line model, respectively. CF: Characteristic frequency.

6.4 Result

6.4.1 Pure tone response

Figure 6.2 shows the IO properties of the simple models and the transmission line model. The input levels were chosen to generate a moderate level of compression.

The IO properties are linear at the lower and higher input levels. The BM displacement of the transmission line model was amplified over 50 dB on the lower input level, in the same way as the linear region in the Neely and Kim model. For the transmission line model, compression depends on the sound frequency. The IO curves are most compressive for the characteristic frequency (most sensitive frequency for the stimuli) and decrease of compression degree for lower input frequency. To evaluate whole cochlear responses from 1000 Hz to 8000 Hz, the slopes values for the IO properties of the transmission line model for CF is calculated over the input range from 30 to 80 dB. Table 6.1 shows the slope values which range from 0.12 to 0.20.

Physiological studies have measured the most compressive growth of the IO properties for the CF and found that the degree of compression decreased when the input frequencies were far from the CF in mammals [52]. The slopes of the IO properties for the moderate input level were 0.1 to 0.2 in the sensitive chinchilla cochlea [59].

6.4.2 Distortion product

Figure 6.3 shows BM displacement for f_1 and f_2 along the cochlear length in the transmission line model. Frequencies f_1 and f_2 were equal to 2850 and 4000 Hz. The peaks of the waves were located 10 and 12 mm from the stapes. Phases for f_1 and f_2 delayed from the base to the apex. This result introduces the forward propagation of waves, known as the traveling wave theory.

Frequencies f_1 and f_2 produced DP $2f_1 - f_2$. The peak amplitude for $2f_1 - f_2$ appeared at 16 mm and is similar to that produced by f_1 and f_2 as input tones. The phase for $2f_1 - f_2$ differed from the phases for f_1 and f_2, and indicated backward and forward wave propagation.

As shown in Fig. 6.3, BM vibration distributed spatially for both the primaries and DP. However, the experimental studies measure the point responses of the BM. To avoid this problem, we evaluated the energy of the BM vibration in terms of the overall response of the BM. According to Ref. [63], the energy of the BM

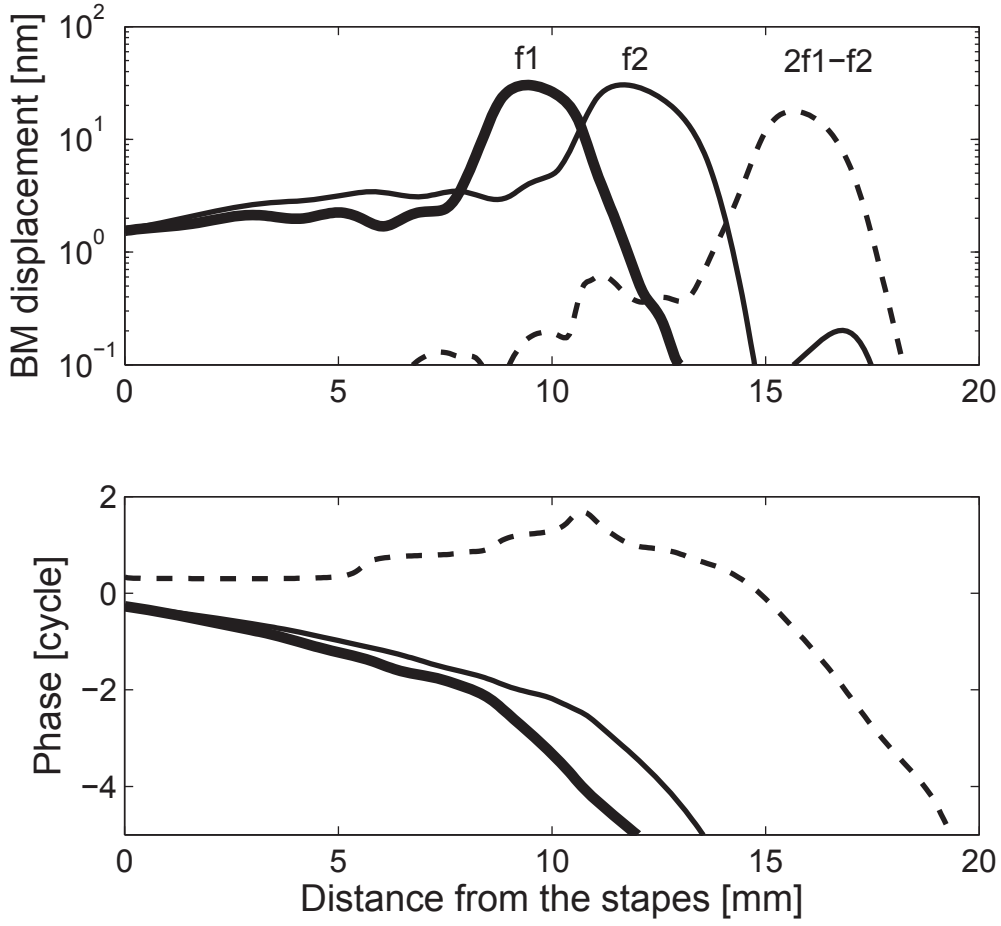

Figure 6.3: Spatial distribution of BM displacement. (Top) Envelopes and (Bottom) phases for the primaries f_1 and f_2 and DP component $2f_1 - f_2$. The thick, thin, and dashed lines indicate displacement for f_1, f_2 and $2f_1 - f_2$, respectively. Frequencies f_1 and f_2 are equal to 2850 and 4000 Hz, respectively.

vibration, $E_b(\omega)$ is given by

$$E_b(\omega) = \frac{1}{2} K(\omega) b^2 \Delta x^2 \sum_{n=1}^{N} |\xi_n^b(\omega)|^2, \tag{6.9}$$

where $K(\omega) = m_1\omega^2$ ($\omega = 2\pi f$) and m_1 is BM mass per unit area. This equation ignores the longitudinal coupling motion reported by Meaud and Grosh [62] because the model does not include the longitudinal coupling of the BM.

Figure 6.4 are isolevel contours of the cubic distortion $2f_1 - f_2$. The input frequencies f_1 and f_2 are 3650 and 4000 Hz ($f_2/f_1 = 1.1$) for the simple models and the power-law nonlinear model and 16 different frequencies f_1 and f_2 for the transmission line model: $f_2 = 1$, 2, 4 and 8 kHz and $f_2/f_1 = 1.4$, 1.3, 1.2 and 1.1.

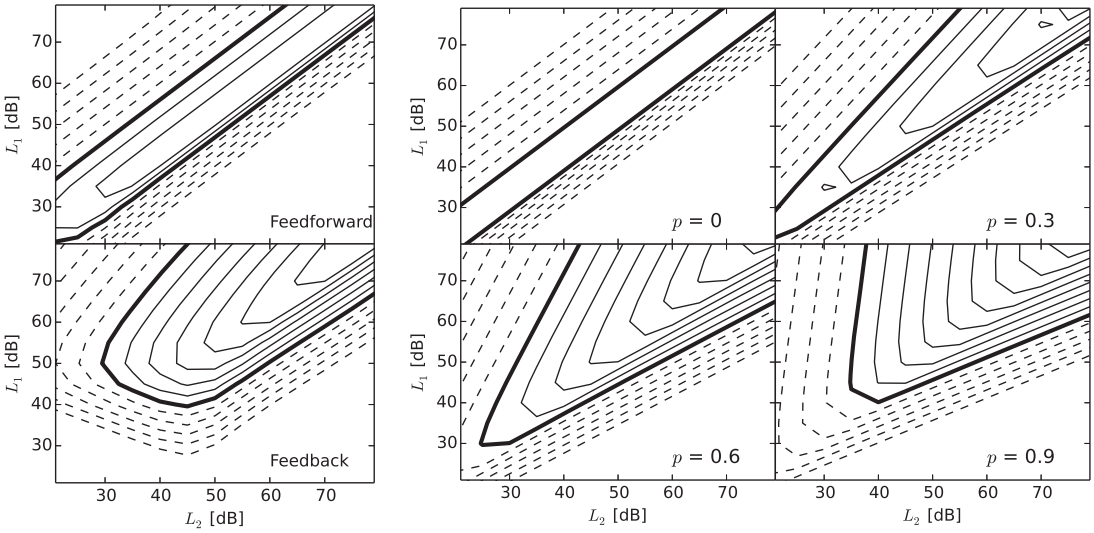

(a) Simple models

(b) Power-law nonlinear model

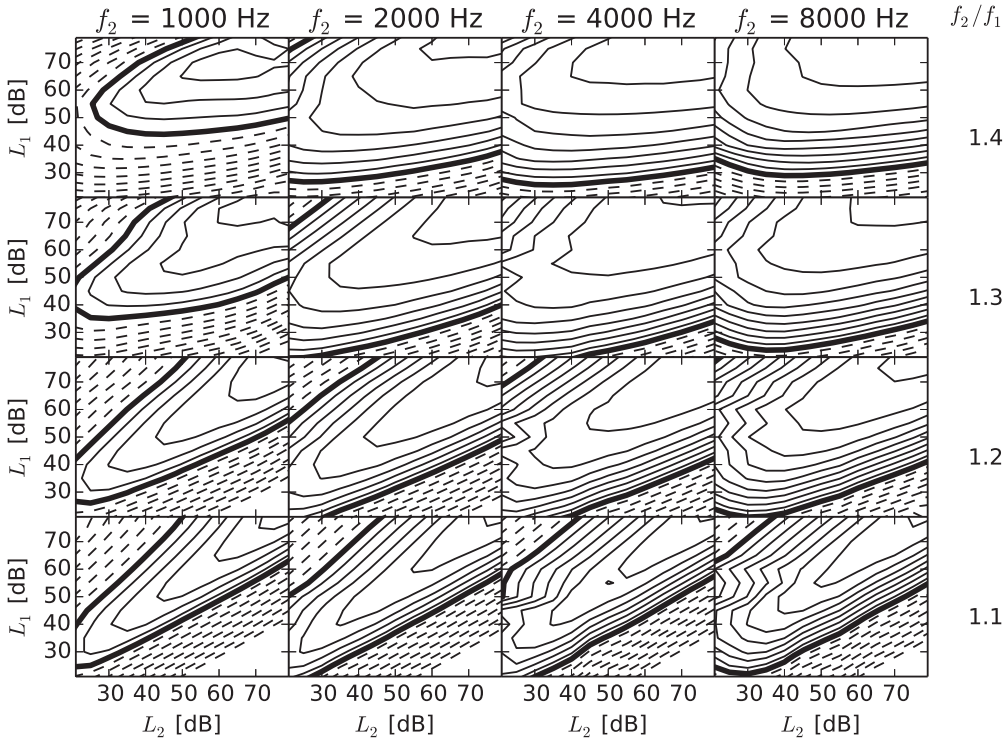

(c) Transmission line model

Figure 6.4: Amplitude of cubic distortion $2f_2 - f1$ as a function of input levels. Iso-output contours are plotted in 4 dB steps. As a reference, the contour corresponding to 0 dB for output is indicated with a thick line. Solid or dashed line represent higher or lower output level, respectively. (a) and (b) Frequencies of the primaries f_1 and f_2 are 3650 and 4000 Hz, respectively. (c) Reference level is 10^{-25} J.

The outputs of the transmission line model are the energy of the BM vibration E_b calculated from Eq. 6.9.

In the simple feedforward model, the contour are oblique that are parallel. In the simple feedback model, the contour are well rounded. The power-law nonlinear model shows that the contour for the lower power p,become more oblique and narrower than for the higher power p. The transmission line model predicts the round contour on the diagonal line. The distribution depends on the frequency ratio f_2/f_1 and is not influenced by frequency f_2. For the lower frequency ratio f_2/f_1, the contour become more oblique and narrower than for the higher frequency ratio f_2/f_1. All models shows that the stripes are narrow where $L_1 > L_2$ and are broad where $L_1 < L_2$.

6.5 Discussion

6.5.1 Comparability of transmission line model and simple models

This paper proposed the simple models categorized to phenomenological models focusing on the nonlinear IO function of the cochlea and the nonlinear transmission line model of the cochlea. In this section, we discuss comparability of the transmission line model and the simple models.

Properties of the present models are the amplification and the saturation where a tone is presented shown in Fig. 6.2. The gain function in the present simple models amplified the input $x(t)$ to 40 dB on the linear region and saturated on the nonlinear region. The active element regarding to the OHC 's motilities in the present transmission line model also amplified BM vibration over 50 dB on the lower sound pressure level condition and reproduced the compression on the moderate input levels.

The simple models amplified both the primaries and distortion in the saturation function G in the Eqs 6.5 and 6.6. The present transmission line model showed the forward traveling waves for the primaries f_1 and f_2 and the forward and backward traveling wave for the distorted $2f_1 - f_2$ where a pair of two tones is presented in Fig. 6.3. The forward traveling wave for a tone are amplified by active element in the cochlea [30] and is similar to the forward traveling waves for the f_1 and f_2. On the other hand, the forward and backward traveling waves for the $2f_1 - f_2$ were generated at $x = 11$ nm. Li and Grosh [76] reported that an internal and

local source could excite both forward and backward traveling waves of the BM. The envelope of the forward traveling wave show a similar shape for the f_1 and f_2. This result indicates that the active element amplifies the spatial responses for the distortion.

6.5.2 Characteristics of DP levels

In this section, we discusses the significance of the saturating feedback to account for the mechanisms that produce DP depending on input level in the cochlea. Measurements of BM vibration in animals [71] and DPOAE [72] showed that DP levels that increased as a function of input levels, had peaks at equal input levels and were sensitive to f_2. The peak amplitudes show the growth with the input levels, and the shapes of curves on the contour map broadened with increments of the frequency ratio f_2/f_1. Liu and Neely showed similar results generated by a saturating feedback within a transmission line model [35].

The amplitudes of DP can be explained that DP amplitude is proportional to input levels in the saturation function as described in Sec. 2.1. However, this cannot explain why the peaks appeared on the diagonal line of Fig. 6.4. We assume that the third-order power series expansion in Eq. 6.1 causes this disagreement with the data.

The mechanoelectric transduction in the OHC shows similar input level dependency for DP in both feedfoward and feedback forms[46, 73], whereas, it was not reported the effect of DP for differences between feedfoward and feedback. The deference between the feedfoward and feedback is degrees of compressive growth in the IO function shown in Fig. 6.2(a). Degree of compressive growth for the simple feedback model is lower than for the simple feedfoward and could be fitted by the power-law nonlinear model in Fig. 6.2(b). The DPs obtained from the simple models in Fig. 6.4(a) are corresponding to those of the power-law nonlinear model in Fig. 6.4(b). This result indicates that the appropriate degree of compressive nonlinearity generated by the saturating feedback affects the DPs depending on input levels.

Complex structure [37] and many parameters [35] in the transmission line models have caused to be difficulties to understand mechanics of DP. In Fig. 6.4, the results obtained from the transmission line model showed similar level dependence of DP to those of the simple feedback model, especially for the higher frequency ratio f_2/f_1. The functions of the simple feedback model are amplification and

saturation realized by one gain factor and one saturation function. Also, the saturating feedback in the present transmission line model affects amplification of the BM motion and have limitation of this amplification. This reason indicates that the saturating feedback generated the level dependence of DP in the transmission line model. The simple models cannot explain the frequency ratio dependence because of the lack of a frequency term in the simple models described in Eqs. 6.5 and 6.6.

6.6 Summary

The modulation effect in the saturation function is a simple and useful explanation of the level dependence of distortion product on the cochlea as a feedforward process. However, cochlear processing has been believed to a saturating feedback process. In the present paper, we proposed simple feedforward and feedback models including one saturation function and one gain factor, a power-law nonlinear model to fit compressive curves, and a transmission line model including a saturating feedback. At moderate input levels, the models show distortion products. The dependence of these distortion products on primary input levels in the simple feedback model is similar to the results obtained from the power-law nonlinear model fitting the compressive growth to the simple feedback models. In addition, those results is shown in the transmission line model. The results suggest that compressive nonlinearity generated by the saturating feedback is dominant to DP and the simple feedback model can account for the details of distortion products in the cochlea.

Chapter 7

Conclusions and further research

In this chapter, we summarize the main conclusions of this thesis and provide some suggestions for further research.

7.1 Conclusions

The cochlea analyzes sound frequency before humans perceive the sound's pitch. This analysis can process varied sounds, softer to louder and low-pitched to high-pitched. Furthermore, the active and nonlinear processes in the cochlea produce this analysis in an elaborate way. To understand how to realize these active and nonlinear processes, isolated cell experiments have shown these processes in the OHCs. Consequently, it is believed that active and nonlinear processes in the OHCs produce the cochlear nonlinearities.

This thesis concentrates on using a model to investigate how the active and nonlinear processes generate cochlear nonlinearities. To do this, we propose a one-dimensional transmission line model of the cochlea, including an active and nonlinear element inspired by the isolated OHC findings. This approach is motivated by the fact that the transmission line model is derived from fundamental physical principles. Consequently, results obtained from the transmission line model can account for the cochlear mechanics. In this thesis, we focus on three typical cochlear nonlinearities: compression, two-tone suppression (2TS), and DP. The results of the computational simulation using the proposed model suggest the mechanisms of the cochlear nonlinearities.

In Chapter 2, we described the structure and response of the auditory peripheral system.

In Chapter 3, we proposed the one-dimensional transmission line model of the

cochlea with feedback via the active and nonlinear OHC model. The active OHC model amplifies the BM motion, and is inspired by both somatic and the hair bundle motility. The shape of the IO property of the OHC is fitted by a second-order Boltzmann function obtained from mechanoelectrical transduction in the OHC.

In Chapter 4, we investigated compression with the proposed model. This model could account for compression obtained from both physiological and psychological experiments. This result was obtained by the saturation of the OHC amplification.

In Chapter 5, we investigated 2TS with the proposed model. The results of the model are comparable to those from 2TS obtained from experimental measurements. To explain this phenomenon, we presented a residual vector concept in the OHC model. This concept was previously shown in the BM motion.

In Chapter 6, we investigated how DP is generated by saturating feedback. We compared three models. The first model was the transmission line model, the second model focused on cochlear saturation processing, and the third model was designed to fit compressive growth in the IO function. These models, with appropriate parameter values, could demonstrate the DP seen in the experimental measurements. These results suggest that the compression produced by the saturating feedback affects DP.

7.2 Suggestions for further research

In this section, we describe suggestions for further research.

1. For cochlear modeling

   Cochlear modeling studies are categorized into two types: transmission line modeling and phenomenological modeling. The former describes the hydrodynamics of the cochlea, and the latter focuses on signal processing in the cochlea. In thesis, we could detect the source of the cochlear nonlinearities such that the saturating effect in the OHC generates an appropriate degree of compression. This concept can be applied to both transmission line and phenomenological modeling. Thus, we can fill the gap between transmission line and phenomenological modeling to better describe cochlear nonlinearities.

2. Model for engineering and medicine

   The prediction of cochlear responses in individual hearing is important in

the fields of engineering and medicine. Particularly when fitting hearing aid systems, an estimation of degree of hearing loss is necessary. Senile and noise-induced hearing losses are caused by the decay of the active and nonlinear OHC function. In this thesis, we tested the cochlear model, including the active and nonlinear function of the OHC, and showed the active and nonlinear mechanisms. Thus, choosing the parameter values of the OHC model leads to the reproduction of the hearing loss, and can clarify the mechanisms of senile and noise-induced hearing losses.

3. For OAE measurement

   OAEs are paid the most attention to as a non-invasive measurement method for cochlear motion and are considered to relate to the active and nonlinear cochlear responses. However, the mechanisms of OAEs are still unclear. In this thesis, we evaluated the overall BM responses to explain the cochlear nonlinearities. Moreover, it is possible that the overall BM responses can account for the active and nonlinear process of OAEs.

References

[1] H. L. F. Helmholtz, *On the Sesations of Tone as a Physiological Basis for the Theory of Music* (London) (1875).

[2] G. Békésy, *Experiments in Hearing* (McGraw-Hill, New York) (1960).

[3] M. C. Libernam and N. Kiang, "Acoustic trauma in cats", Acta Otolaryngologica **358**, 1–63 (1978).

[4] P. M. Sellick, R. Patuzzi, and B. M. Johnstone, "Measurement of basilar membrane motion in the guinea pig using the mossbauer technique", Journal of Acoustical Society of America **72**, 131–141 (1982).

[5] S. S. Narayan, "Frequency Tuning of Basilar Membrane and Auditory Nerve Fibers in the Same Cochleae", Science **282**, 1882–1884 (1998).

[6] W. E. Brownell, C. R. Bader, D. Bertrand, and Y. de Ribaupierre, "Evoked mechanical responses of isolated cochlear outer hair cells", Science **227**, 194 – 196 (1985).

[7] J. F. Ashmore, "A fast motile response in guinea-pig outer hair cells: the cellular basis of the cochlear amplifier", Journal of Physiology **388**, 323–347 (1987).

[8] P. Dallos, "The active cochlea", J neurosci **2** (1992).

[9] M. C. Liberman, J. Gao, D. Z. Z. He, X. Wu, S. Jia, and J. Zuo, "Prestin is required for electromotility of the outer hair cell and for the cochlear amplifier", Nature **419** (2002).

[10] H. J. Kennedy, A. C. Crawford, and R. Fettiplace, "Force generation by mammalian hair bundles supports a role in cochlear amplification", Nature **433**, 880 – 883 (2005).

[11] A. J. Hudspeth, "Review Making an Effort to Listen : Mechanical Amplification in the Ear", Neuron 530–545 (2008).

[12] A. W. Peng and A. J. Ricci, "Somatic motility and hair bundle mechanics , are both necessary for cochlear amplification ?", Hearing Research **273**, 109–122 (2011).

[13] W. S. Rhode, "Basilar membrane mechanics in the 6 kHz region of sensitive chinchilla cochleae", The Journal of the Acoustical Society of America **121**, 2792 (2007).

[14] N. P. Cooper, "Compression in the peripheral auditory system", in *Compression*, edited by S. Bacon and R. R. Fay (Springer, New York) (2004).

[15] C. J. Plack and a. J. Oxenham, "Basilar-membrane nonlinearity estimated by pulsation threshold.", The Journal of the Acoustical Society of America **107**, 501–7 (2000).

[16] N. Kiang, *Discharge patterns of single fibers in the cat's auditory nerve* (M.I.T. Press) (1965).

[17] M. A. Ruggero, L. Robles, and N. C. Rich, "Two-tone suppression in the basilar membrane of the cochlea: mechanical basis of auditory-nerve rate suppression", Journal of Neurophysiology **68**, 1087–1099 (1992).

[18] P. M. Sellick and I. J. Russell, "Two-tone suppression in cochlear hair cells", Hearing Research **1**, 227–236 (1976).

[19] J. Goldstein and N. Kiang, "Neural Correlates of the Aural Combination Tone $2f_1 - f_2$ ", Proceedings of the IEEE **56** (1968).

[20] S. A. Gaskill and A. M. Brown, "The behavior of the acoustic distortion product, 2f1-f2, from the human ear and its relation to auditory sensitivity.", The Journal of the Acoustical Society of America **88**, 821–39 (1990).

[21] L. Robles, M. A. Ruggero, and N. C. Rich, "Two-tone distortion in the basialr membrane of the cochlea", Nature **349**, 413–414 (1991).

[22] L. Robles, M. A. Ruggero, and N. C. Rich, "Two-tone distortion on the basilar membrane of the chinchilla cochlea.", Journal of neurophysiology **77**, 2385–2399 (1997).

[23] M. C. Liberman, J. Zuo, and J. J. Guinan, "Otoacoustic emissions without somatic motility: Can stereocilia mechanics drive the mammalian cochlea?", The Journal of the Acoustical Society of America **116**, 1649 (2004).

[24] M. a. Cheatham, K. H. Huynh, J. Gao, J. Zuo, and P. Dallos, "Cochlear function in Prestin knockout mice.", The Journal of physiology **560**, 821–30 (2004).

[25] M. Drexl, M. M. M. Lagarde, J. Zuo, A. N. Lukashkin, and I. J. Russell, "The role of prestin in the generation of electrically evoked otoacoustic emissions in mice.", Journal of neurophysiology **99**, 1607–15 (2008).

[26] J. J. Zwislocki, "Theory of the acoustical action of the cochlea", Journal of Acoustical Society of America **22**, 778–784 (1950).

[27] L. C. Peterson and B. P. Bogert, "A dynamicsl theory of the cochlea", Journal of Acoustical Society of America **22**, 369–381 (1950).

[28] E. de Boer, "No sharpening? a challenge for cochlea mechanics", Journal of Acoustical Society of America **73**, 567–573 (1983).

[29] S. T. Neely and D. O. Kim, "An active cochlear model showing sharp tuning and high sensitivity", Hearing Research **9**, 123–130 (1983).

[30] S. Neely and D. Kim, "A model for active elements in cochlear biomechanics", The journal of the acoustical society of America **79**, 1472–1480 (1986).

[31] E. Zwicker, "Suppression and (2f1-f2)-difference tones in a nonlinear cochlear preprocessing model with active feedback.", The Journal of the Acoustical Society of America **80**, 163–76 (1986).

[32] L. Kanis and E. de Boer, "Two- tone suppression in a locally active nonlinear model of the cochlea", The Journal of the Acoustical Society of America **96**, 2156–2165 (1994).

[33] R. S. Chadwick, "Compression, gain, and nonlinear distortion in an active cochlear model with subpartitions.", Proceedings of the National Academy of Sciences of the United States of America **95**, 14594–9 (1998).

[34] K.-M. Lim and C. R. Steele, "A three-dimensional nonlinear active cochlear model analyzed by the WKB-numeric method.", Hearing research **170**, 190–205 (2002).

[35] Y.-W. Liu and S. T. Neely, "Distortion product emissions from a cochlear model with nonlinear mechanoelectrical transduction in outer hair cells.", The Journal of the Acoustical Society of America **127**, 2420–32 (2010).

[36] B. Epp, J. L. Verhey, and M. Mauermann, "Modeling cochlear dynamics: interrelation between cochlea mechanics and psychoacoustics.", The Journal of the Acoustical Society of America **128**, 1870–1883 (2010).

[37] J. a. How, S. J. Elliott, and B. Lineton, "The influence on predicted harmonic and distortion product generation of the position of the nonlinearity within cochlear micromechanical models.", The Journal of the Acoustical Society of America **127**, 652–5 (2010).

[38] H. Fletcher, "Auditory patterns", Reviews of Modern Physics **12**, 47–65 (1940).

[39] R. Meddis, L. P. O'Mard, and E. a. Lopez-Poveda, "A computational algorithm for computing nonlinear auditory frequency selectivity", The Journal of the Acoustical Society of America **109**, 2852–2861 (2001).

[40] X. Zhang, M. G. Heinz, I. C. Bruce, and L. H. Carney, "A phenomenological model for the responses of auditory-nerve fibers: I. Nonlinear tuning with compression and suppression", The Journal of the Acoustical Society of America **109**, 648–670 (2001).

[41] J. O. Pickles, *An Introduction to the Physiology of Hearing* (Emerald Group Publishing, Bingley) (2008).

[42] N. B. Slepecky, "Structure of the mammalian cochlea", in *The cochlea*, edited by P. Dallos, A. N. Popper, and R. R. Fay (Springer, New York) (1996).

[43] C. Giguere and P. Woodland, "A computational model of the auditory periphery for speech and hearing research. I. Ascending path", Journal of the Acoustical Society of America **95**, 331–342 (1994).

[44] S. J. Elliott, E. M. Ku, and B. Lineton, "A state space model for cochlear mechanics.", The Journal of the Acoustical Society of America **122**, 2759–71 (2007).

[45] E. M. Ku, S. J. Elliott, and B. Lineton, "Statistics of instabilities in a state space model of the human cochlea", The Journal of the Acoustical Society of America **124**, 1068 (2008).

[46] a. N. Lukashkin and I. J. Russell, "A descriptive model of the receptor potential nonlinearities generated by the hair cell mechanoelectrical transducer.", The Journal of the Acoustical Society of America **103**, 973–80 (1998).

[47] D. Greenwood, "A cochlear frequency-position function for several species—29 years later", The Journal of the Acoustical Society of America **87**, 2592 (1990).

[48] R. Diependaal, H. Duifhuis, H. Hoogstraten, and M. Viergever, "Numerical methods for solving one-dimensional cochlear models in the time domain", The Journal of the Acoustical Society of America **82**, 1655 (1987).

[49] M. L. Jepsen and T. Dau, "Behavioral estimates of basilar-membrane input-output functions in normal-hearing listeners", in *Proc. FORUM ACUSTICA*, 2679–2683 (2011).

[50] E. a. Lopez-Poveda and R. Meddis, "A human nonlinear cochlear filterbank", The Journal of the Acoustical Society of America **110**, 3107 (2001).

[51] R. Patterson, M. Allerhand, and C. Giguere, "Time-domain modeling of peripheral auditory processing: A modular architecture and a software platform", JOURNAL-ACOUSTICAL SOCIETY OF AMERICA **98**, 1890–1890 (1995).

[52] L. Robles and M. a. Ruggero, "Mechanics of the mammalian cochlea.", Physiological reviews **81**, 1305–52 (2001).

[53] B. C. J. Moore, *An introduction to the psychology of hearing* (Emerald Group Publishing, Bingley) (2012).

[54] R. D. Patterson, M. Unoki, and T. Irino, "Extending the domain of center frequencies for the compressive gammachirp auditory filter", The Journal of the Acoustical Society of America **114**, 1529 (2003).

[55] J. Goldstein, "Auditory nonlinearity", The Journal of the Acoustical Society of America **41**, 676–689 (1967).

[56] W. M. Roberts and M. a. Rutherford, "Linear and nonlinear processing in hair cells.", The Journal of Experimental Biology **211**, 1775–1780 (2008).

[57] C. D. Geisler and a. L. Nuttall, "Two-tone suppression of basilar membrane vibrations in the base of the guinea pig cochlea using "low-side" suppressors.", The Journal of the Acoustical Society of America **102**, 430–440 (1997).

[58] N. P. Cooper, "Two-tone suppression in cochlear mechanics.", The Journal of the Acoustical Society of America **99**, 3087–98 (1996).

[59] W. S. Rhode, "Mutual suppression in the 6 kHz region of sensitive chinchilla cochleae", The Journal of the Acoustical Society of America **121**, 2805–2818 (2007).

[60] B. Delgutte, "Two-tone rate suppression in auditory-nerve fibers: dependence on suppressor frequency and level.", Hearing research **49**, 225–46 (1990).

[61] T. Ren, W. He, and P. Gillespie, "Measurement of cochlear power gain in the sensitive gerbil ear", Nature communications **2** (2011).

[62] J. Meaud and K. Grosh, "The effect of tectorial membrane and basilar membrane longitudinal coupling in cochlear mechanics.", The Journal of the Acoustical Society of America **127**, 1411–1421 (2010).

[63] J. L. Meriam and L. G. Kraige, *Engineering mechanics: Dynamics* (Willey, New York) (2012).

[64] E. de Boer and A. Nuttall, "The mechanical waveform of the basilar membrane. III. Intensity effects", The Journal of the Acoustical Society of America **107**, 1497–1507 (2000).

[65] M. A. Cheatham, "Comment on "Mutual suppression in the 6 kHz region of sensitive chinchilla cochleae" [J. Acoust. Soc. Am. 121, 2805-2818 (2007)].", The Journal of the Acoustical Society of America **123**, 602–605 (2008).

[66] R. Nobili and F. Mammano, "Biophysics of the cochlea. II: Stationary nonlinear phenomenology.", The Journal of the Acoustical Society of America **99**, 2244–2255 (1996).

[67] S. Ramamoorthy, N. V. Deo, and K. Grosh, "A mechano-electro-acoustical model for the cochlea: Response to acoustic stimuli", The Journal of the Acoustical Society of America **121**, 2758–2773 (2007).

[68] H. Cai, B. Shoelson, and R. S. Chadwick, "Evidence of tectorial membrane radial motion in a propagating mode of a complex cochlear model.", Proceedings of the National Academy of Sciences of the United States of America **101**, 6243–6248 (2004).

[69] F. Jülicher, D. Andor, and T. Duke, "Physical basis of two-tone interference in hearing.", Proceedings of the National Academy of Sciences of the United States of America **98**, 9080–9085 (2001).

[70] R. Szalai, A. Champneys, M. Homer, D. Ó Maoiléidigh, H. Kennedy, and N. Cooper, "Comparison of nonlinear mammalian cochlear-partition models.", The Journal of the Acoustical Society of America **133**, 323–36 (2013).

[71] N. P. Cooper and W. S. Rhode, "Mechanical responses to two-tone distortion products in the apical and basal turns of the mammalian cochlea.", Journal of neurophysiology **78**, 261–70 (1997).

[72] T. A. Johnson, S. T. Neely, C. A. Garner, and M. P. Gorga, "Influence of primary-level and primary-frequency ratios on human distortion product otoacoustic emissions", The Journal of the Acoustical Society of America **119**, 418 (2006).

[73] A. N. Lukashkin and I. J. Russell, "Analysis of the f2-f1 and 2f1-f2 distortion componets generated by the hair cell mechanoelectrical transducer: Dependence on the amplitudes of the primaries and feedback gain", The Journal of the Acoustical Society of America **106**, 2661–2668 (1999).

[74] N. P. Cooper, "Harmonic distortion on the basilar membrane in the basal turn of the guinea-pig cochlea.", The Journal of physiology **509 (Pt 1**, 277–88 (1998).

[75] C. P. C. Versteegh and M. van der Heijden, "Basilar Membrane Responses to Tones and Tone Complexes: Nonlinear Effects of Stimulus Intensity.", Journal of the Association for Research in Otolaryngology **2040** (2012).

[76] Y. Li and K. Grosh, "Direction of wave propagation in the cochlea for internally excited basilar membrane", The Journal of the Acoustical Society of America **131**, 4710 (2012).

Publications

Journal papers

1. **Yasuki Murakami**i and Shunsuke Ishimitsu, "Distortion product level dependency generated by saturating feedback in a cochlear model" *Acoustical Science and Technology* （印刷中）
2. **Yasuki Murakami** and Shunsuke Ishimitsu, "Relationship between psychologically estimated cochlear input-output functions and physiologogical functions" *ICIC Express Letters*, pp.1737-1742, June,2013.
3. **Yasuki Murakami**i and Shunsuke Ishimitsu, "An active and nonlinear element for two-tone suppression in basilar membrane" （投稿準備中)
4. **Yasuki Murakami** and Shunsuke Ishimitsu, "Comparison of state space models for cochlear network" (投稿準備中)

International conference papers

1. **Yasuki Murakami** and Shunsuke Ishimitsu, "A Model for Difference Between Two-Suppression and Distortion Product in The Basilar Membrane," The Proc. of The 21th International Congress on Sound and Vibration, paper number 811, July, 2014
2. **Yasuki Murakami** and Shunsuke Ishimitsu, "Modeling Two-tone Suppression and Distortion Product on Basilar Membrane," Proc. Mechanics of Hearing 12th International Workshop, pp. 469-473, June, 2014

3. **Yasuki Murakami** and Shunsuke Ishimitsu, “Two-Tone Suppression Based on Somatic Motility of the Outer Hair Cell with a Cochlear Model,” ARO 36th Annual MidWinter Meeting, Vol. 36, pp. 507, Feb., 2013.
4. **Yasuki Murakami** and Shunsuke Ishimitsu, “Relationship between psychologically estimated cochlear input-output functions and physiological functions”, The 7th International conference on Innovative Computing, Information and Control, Nov. 2012.
5. **Yasuki Murakami** and Shunsuke Ishimitsu, “Generation Mechanisms of Two-Tone Suppression using a cochlear model,” Proc. AES 45th International Conference, pp. 333-341, Mar. 2012.

Domestic conference papers

1. **Yasuki Murakami** and Shunsuke Ishimitsu “Feedback from outer hair cells generates distortion product on basilar membrane,” 日本音響学会聴覚研究会資料，Vol.44 No.4 H-2014-32, May, 2014
2. 村上泰樹，石光俊介 “基底膜振動系での 2 音抑圧に与える 2 次元的圧縮特性の影響,” 日本音響学会春季研究発表会，2-8-6，Mar.，2013
3. 村上泰樹，石光俊介 “心理学的に推定される聴覚系の入出力特性の生理学的メカニズム,” 日本音響学会騒音・振動研究会，N-2013-03，Jan.，2013
4. 村上泰樹，石光俊介 “聴覚末梢系での非線形現象の説明のためのモデルの提案,” 統計数理研究所共同研究集会「医学・工学における逆問題とその周辺 (4)」, Nov., 2012
5. 村上泰樹，石光俊介 “基底膜振動系での圧縮特性と二音抑圧の相関性,” 日本音響学会秋季研究発表会，3-3-6, Sep., 2012
6. 村上泰樹，石光俊介 “外有毛細胞の細胞体運動に着目した蝸牛モデルの二音抑圧のメカニズム，” Dynamic and Design Conference 2012, 432, Sep. 2012

7. 村上泰樹，石光俊介 “細胞体運動に着目した蝸牛での二音抑圧のメカニズム,” 日本音響学会聴覚研究会資料，Vol.42, No.3, H-2012-47, May，2012
8. 村上泰樹，石光俊介 “ 抑圧の影響を考慮した蝸牛モデルの入出力特性の検討，” 日本音響学会春季研究発表会，3-Q-23, Mar., 2012
9. 村上泰樹，石光俊介 “蝸牛モデルを用いた二音抑圧に対する外有毛細胞の影響，” 日本音響学会春季研究発表会，3-10-1, Mar., 2012